Journal of Materials Chemistry C

ROYAL SOCIETY OF CHEMISTRY

REVIEW

View Article Online
View Journal | View Issue

Cite this: J. Mater. Chem. C, 2023, 11, 8688

Design, synthesis and functionalization of BODIPY dyes: applications in dye-sensitized solar cells (DSSCs) and photodynamic therapy (PDT)

Indresh Singh Yadav and Rajneesh Misra *

In recent years, BODIPY dyes have emerged as a valuable category of luminogens for optoelectronic applications because of their spectacular properties, such as good fluorescence quantum yield, broad absorption with high molar extinction coefficient, excellent photo-chemical and thermal stability, remarkable redox properties, easy structural modifications and good solubility. These properties of BODIPY dyes make them an important class of chromophores for application in nonlinear optics, dye-sensitized solar cells, chemosensors, photodynamic therapy, bioimaging, electron-transporting materials, ultrafast charge transfer, perovskite solar cells and many more. BODIPY dyes have three main reactive sites: α-, β-pyrrolic and *meso* positions, which enable modifications for the synthesis of various donor–acceptor BODIPY dyes. BODIPY derivatives that exhibit high thermal and photostability, low-cost production, strong NIR absorption/emission and a low bandgap have been explored for photovoltaic and biomedical applications. In this review, we discuss the synthesis, functionalization, and various reactions, such as Pd-catalyzed cross-coupling reactions, Grignard reactions, the Knoevenagel reaction and many more, at the α-, β-pyrrolic and *meso* positions of the BODIPY core and the application of BODIPY dyes in dye-sensitized solar cells and photodynamic therapy.

Received 15th January 2023,
Accepted 25th May 2023

DOI: 10.1039/d3tc00171g

rsc.li/materials-c

1. Introduction

The development of novel multi-modular conjugated D–A chromophores has attracted interest from the scientific community due to their wide range of applications in organic solar cells,

Department of Chemistry, Indian Institute of Technology, Indore 453552, India.
E-mail: rajneeshmisra@iiti.ac.in

Indresh Singh Yadav

Indresh Singh Yadav is pursuing his PhD at the Indian Institute of Technology (IIT) Indore (M.P.), India, under the supervision of Prof. Rajneesh Misra. He completed his MSc degree in 2016 and BSc degree in 2014 at Feroze Gandhi College, Raebareli (U.P.), India. Currently he is working on the design and synthesis of BODIPY-based donor–acceptor chromophores for optoelectronic applications.

Rajneesh Misra

Prof. Rajneesh Misra is currently working as a Professor at the Department of Chemistry, Indian Institute of Technology, Indore (IIT-Indore). He obtained his master's degree from the University of Gorakhpur, India, in 2001. He moved to the Indian Institute of Technology, Kanpur, for his PhD in Chemical Sciences (2007). After two successive postdoctoral positions, at the Georgia Institute of Technology, Atlanta, USA, from 2007 to 2008, and at Kyoto University, Japan, from 2008 to 2009, he joined IIT Indore, India, in 2009 as an Assistant Professor. His research interests lie in the areas of organic photonics and organic electronics.

organic photovoltaics, thermally activated delayed fluorescence (TADF), non-linear optics (NLOs) as well as in biological studies.[1–8] Such D–A-based chromophores, which exhibit high thermal and photochemical stability, broad absorption in the UV-vis range and narrow bandgaps, are potential candidates for optoelectronic applications.[9] The D–A strategy has been used for the development of NIR-absorbing/emitting materials with a narrow HOMO–LUMO gap.[10] The optoelectronic properties of D–A chromophores can be easily tuned by (a) adjusting the π-linker between the donor and acceptor units or (b) choosing the appropriate electron donor/acceptor unit in the molecular system.[11–14] Using a suitable π-linker (such as a double or triple bond or an aromatic ring), the hybridization between donor and acceptor moieties significantly perturbs the HOMO–LUMO energy levels.[15,16] The D–A strength, which is dependent on the type of donor group, acceptor group as well as the type of π-linker/spacer unit, plays a significant role in the development of D–A systems.[17] D–A chromophores with a low bandgap exhibit potential applications in DSSCs,[18] bulk heterojunction organic solar cells (BHJOSCs),[19] NLOs,[20] organic field effect transistors (OFETs),[21] bioimaging[22] and photodynamic therapy.[23]

1.1. BODIPY

Dipyrromethene (or dipyrrin) is a bidentate ligand with *cis* and *trans* isomeric forms. BODIPY is highly planar; however, the boron atom is slightly distorted from the normal plane in some cases.[24] BF_2-chelated dipyrromethenes have received considerable interest from the scientific community as a building component for artificial photosynthetic systems, light-harvesting arrays, fluorescent switches, tunable laser dyes, molecular probes and many more uses.[25–30] BODIPY is an electron-deficient (acceptor) molecule; therefore, incorporating an electron-donating (donor) group induces a donor–acceptor interaction in the molecular system. In 1968, Treibs and Kreuzer synthesized BODIPY, which exhibits pyrrole, azafulvene and diazaborinine-type rings in the π-conjugated system.[31] The IUPAC numbering for the 4,4-difluoro-4-bora-3*a*,4*a*-diaza-*s*-indacene (BODIPY) dye differs from that of dipyrromethene (Fig. 1). These naming approaches have been broadly accepted and are frequently used in the current literature. The BODIPY core can be modified easily to fine-tune the photonic and electronic properties. The BODIPY core can also be functionalized at the α-, β- and *meso* positions, as well as at the B(III) center *via* incorporating various substituents and altering the conjugation length using a suitable spacer or π-linker unit. BODIPY dyes (BODIPYs) are one of the most studied organic fluorophores due to their extensive functionalization and tunable photonic and electronic properties. A wide range of BODIPY intermediates with reactive functionalities (halogen, alkylthio, methyl, formyl) have been used to synthesize various BODIPY derivatives *via* Pd-catalyzed cross-coupling reactions, condensation reactions, direct styrylation, nucleophilic substitution and [2+2] cycloaddition–retroelectrocyclization reactions for photovoltaic and biological applications. BODIPY fluorophores exhibit excellent properties, such as high absorption

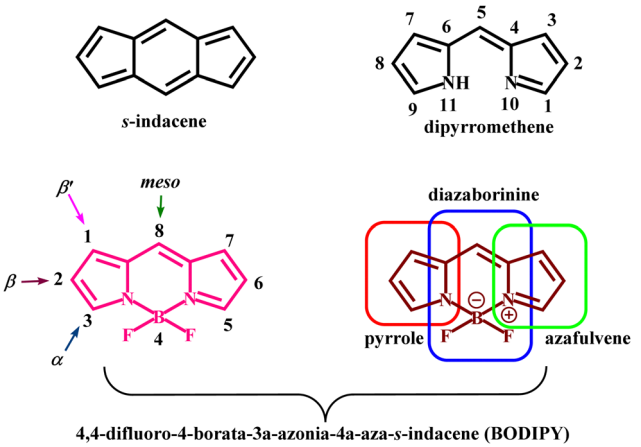

Fig. 1 Nomenclature of *s*-indacene, dipyrromethene and the BODIPY core.

coefficients, strong fluorescence, high thermal and chemical stability, good solubility, resistance towards self-aggregation, among others.[32–38] These properties make them unique and useful candidates for organic electronics, chemosensors, photovoltaics, photodynamic therapy and bioimaging applications.[39–45]

BODIPYs generally exhibit a strong absorption band around 500–550 nm (ε = 40 000–80 000 M^{-1} cm^{-1}) corresponding to the $S_0 \rightarrow S_1$ transition (π–π*) and a shoulder peak in the lower wavelength region due to a vibrational transition.[46,47] BODIPY exhibits an absorption band around 350–380 nm, which corresponds to the $S_0 \rightarrow S_2$ transition (π–π*) and emits a narrow spectrum between 530 and 560 nm.[48,49] BODIPY derivatives exhibit good photochemical stability and solubility in common organic solvents.[50] The BODIPY fluorophore exhibits high electron affinity, making it an excellent acceptor in D–A-type molecular systems.[51] The photonic and electronic properties of BODIPYs can be perturbed by incorporating a suitable substituent at the α-, β- and *meso*-positions of BODIPY unit.[52] The excellent optical properties and easy synthetic modification of BODIPYs make them the most studied fluorophore, and they have been used as a potential candidate in dye-sensitized solar cells, sensors, photosensitizers, fluorescent switches, nonlinear optics, photodynamic therapy (PDT), laser dyes, light harvesting and bioimaging applications.[53–60] Normal BODIPYs exhibit an absorption in the green spectral region (about 500 nm), which is not appropriate for *in vivo* PDT. Alternatively, near-IR absorption is desired for *in vivo* PDT because light with such wavelengths enables deeper tissue penetration.[61] Photosensitizers are an important part of photodynamic therapy, and a good photosensitizer will possess a long excitation wavelength, NIR fluorescence emission, low cytotoxicity, good photostability and a high $^1O_2$ quantum yield. Therefore, the D–A/D–π–A approach promotes efficient intramolecular charge transfer (ICT), which causes a redshift in the spectrum as well as a decrease in the energy gap (E_g) between the HOMO and the LUMO, which increases the $^1O_2$ quantum yield.[62]

1.2. Synthesis of the BODIPY core

The methodologies for synthesizing BODIPY are mentioned in the following sections. In 1968, Treibs and Kreuzer accidentally discovered the typically strong fluorescent F-BODIPY framework while attempting to acylate 2,4-dimethylpyrrole with excess acetic anhydride and $BF_3{\cdot}OEt_2$ (with the Lewis acid as the catalyst). The brightly colored mono- and di-substituted BODIPYs **1** and **2**, respectively, were isolated in <10% yield. The chelation of dipyrrin with BF_2 facilitates the tetrahedral geometry at the boron center (Scheme 1).[31]

1.2.1. From aldehyde and pyrrole. BODIPYs have been synthesized *via* the Lindsey method. This approach is based on the acid-catalyzed condensation reaction of pyrrole and benzaldehyde. The final product was obtained in 22% yield using DDQ and $BF_3{\cdot}OEt_2$ (Scheme 2). BODIPY **3** exhibits an absorption band at 503 nm in toluene.[63]

1.2.2. From pyrrole and acid chloride. In 2012, Zhang *et al.* reported a facile one-pot synthesis of BODIPY **4** in 21% yield *via* the reaction of pyrrole and acid chloride followed by the complexation reaction with $BF_3{\cdot}OEt_2$ (Scheme 3). BODIPY **4** shows an absorption band at 494 and an emission band at 512 nm; it also exhibits a high fluorescence quantum yield (0.87) and a long fluorescence lifetime in dichloromethane (DCM) solvent.[64,65]

1.2.3. From substituted pyrrole-2-carbaldehyde. BODIPY dyes have been synthesized from the self-condensation reaction between pyrrole-2-carbaldehyde and $POCl_3$ followed by TEA and $BF_3{\cdot}OEt_2$. The 5-*tert*-butyl-pyrrole-2-carbaldehyde was used to synthesize BODIPY **5** in 15% yield (Scheme 4). BODIPY **5** exhibits a narrow absorption band at a higher wavelength (492–500 nm), which is assigned to the $S_0 \rightarrow S_1$ transition, and a band at a shorter wavelength, which is assigned to the $S_0 \rightarrow S_2$ transition.[66]

1.2.4. From pyrrole and triethyl orthoformate. In 2014, Kolemen *et al.* reported BODIPY **6**, synthesized using 2,4-dimethylpyrrole, triethyl orthoformate, $POCl_3$ and a complexation reaction with $BF_3{\cdot}OEt_2$ at 40 °C, which resulted in a 40% yield (Scheme 5).[67]

1.2.5. From pyrrole and thiophosgene. In 2012, Kim *et al.* reported the synthesis of BODIPY **7** and used this as an intermediate to form BODIPY **8** for the ratiometric fluorescence sensing of Hg^{2+} ions. BODIPY **8** undergoes Hg^{2+} promoted hydrolysis to produce 8-hydroxy-BODIPY, which is accompanied by a large change in the emission wavelength.[68] In 2019, Chi *et al.* synthesized BODIPY **8** using pyrrole and thiophosgene. The pyrrole reacts with $CSCl_2$ in the presence of DCM or toluene solvent, which results in the intermediate bis-(1*H*-pyrrol-2-yl)-methanethione. The bis-(1*H*-pyrrol-2-yl)-methanethione was reacted further with methyl iodide followed by triethylamine and $BF_3{\cdot}OEt_2$, resulting in BODIPY **8** in 26% yield (Scheme 6). BODIPY **8** exhibits an absorption band at 485 nm and emission band at 525 nm. Bright green fluorescence can be seen in a solution of BODIPY **8**; however, after being exposed to $HgCl_2$, blue fluorescence was produced.[69] Recently, Dehaen and co-workers also reported a procedure for the design and synthesis of *meso*-halo BODIPYs *via* dipyrryl thione (7) as shown in Scheme 10.[70]

1.2.6. From substituted pyrroles. In 2012, Boens *et al.* reported the synthesis of BODIPY **9** using substituted pyrroles followed by complexation with TEA and $BF_3{\cdot}OEt_2$ (Scheme 7). BODIPY **9** consists of two cyclohexane rings fused at the 2,3- and 5,6-positions. In addition, BODIPY **9** exhibits an absorption at 534–543 nm and an emission band at 543–551 nm with a high fluorescence quantum yield of 0.76–0.89.[71]

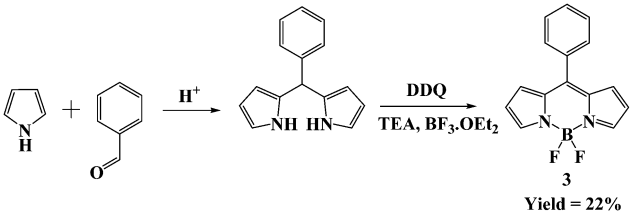

Scheme 2 Lindsey method for the synthesis of BODIPY **3**.

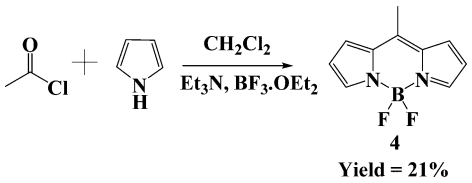

Scheme 3 Synthesis of BODIPY **4** from pyrrole and acid chloride.

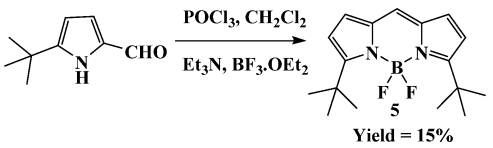

Scheme 4 Synthesis of BODIPY **5** from 5-*tert*-butyl-pyrrole-2-carbaldehyde.

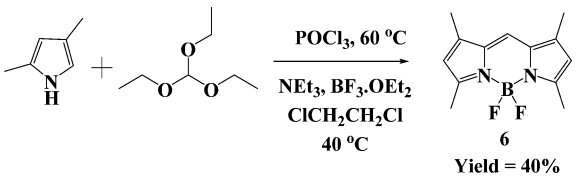

Scheme 5 Synthesis of BODIPY **6** from 2,4-dimethylpyrrole and triethyl orthoformate.

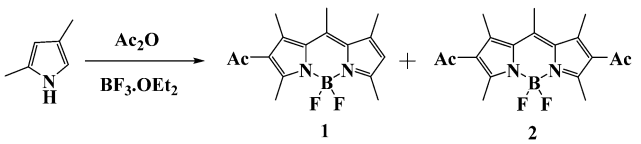

Scheme 1 Synthesis of the BODIPYs **1** and **2** from the 2,4-dimethylpyrrole.

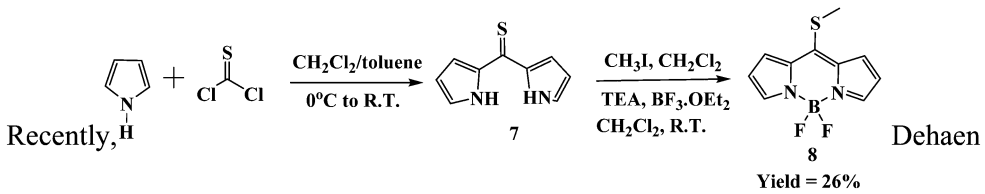

Scheme 6 Synthesis of BODIPY **7** and **8** from pyrrole and $CSCl_2$.

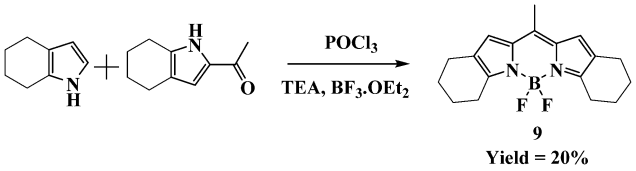

Scheme 7 Synthesis of BODIPY **9** from substituted pyrroles.

1.3. Functionalization of the BODIPY core

The spectroscopic and photophysical properties can be fine-tuned by adding appropriate groups to the BODIPY core at the correct positions. Boron dipyrrin dyes can be functionalized easily at the pyrrole C-ring positions, the *meso*-position and at the boron atom.[72]

There are many different functionalization methods that can be utilized in order to derivatize the BODIPY framework. Significant progress has been made in functionalizing the BODIPY dyes at different pyrrolic positions *via* nucleophilic substitution, Knoevenagel-type condensation reactions, substitution of the fluorine atoms on boron, direct styrylation, nucleophilic substitution at the *meso*-position, Libenskid cross-coupling and metal-catalyzed C–C coupling reactions (Fig. 2).[73] All of these methods can be used to synthesize BODIPY derivatives to tune the optoelectronic properties. The design and synthesis of donor–acceptor-based BODIPYs has been used widely for developing NIR-absorbing materials for PDT applications, as well as those with a low bandgap value and improved power conversion efficiency for DSSCs. Expansion of the π-conjugation is a primary method to enhance the absorption band from the visible to the NIR region and for improving the J_{SC} value of DSSCs.[74] Fukuzumi *et al.* reported D–A BODIPY dyes that exhibit a low fluorescence quantum yield due to photoinduced electron transfer (PeT) from the trimethoxybenzene donor to the BODIPY acceptor.[75]

1.3.1. Halogenation

1.3.1.1. Halogenation reaction at the α-position of BODIPY. In 2006, Rohand *et al.* reported the α-chloro-functionalized BODIPYs **10** and **11** (Scheme 8).[76] A benzaldehyde derivative was reacted with pyrrole and a catalytic amount of trifluoroacetic acid to form the dipyrromethane. Chlorination occurred selectively at the α-position of the dipyrromethane upon varying the number of equivalents of *N*-chlorosuccinimide (NCS).

The dipyrromethane was treated with NCS/NBS and DDQ, followed by complexation with TEA and $BF_3{\cdot}OEt_2$ which resulted in α-chloro- or α-bromo-substituted BODIPYs in good yields.[76,77] BODIPYs **10** and **11** were synthesized using 2 and 14 equivalents of *N*-chlorosuccinimide in the presence THF solvent followed by complexation with $BF_3{\cdot}Et_2O$, in 20% and 22% yields, respectively (Scheme 8). The α-brominated BODIPYs **12**–**17** were synthesized by reacting dipyrromethane with 1–10 equivalents of *N*-bromosuccinimide (NBS), resulting in yields of 16–40% (Scheme 8).

1.3.1.2. Halogenation reaction at the β-position of BODIPY. BODIPYs undergo electrophilic substitution reactions at the BODIPY β-pyrrolic positions. Different procedures have been reported in the literature in which the BODIPY can be chlorinated, brominated and iodinated to obtain β-halogenated BODIPYs in good yields. Halogenating reagents such as NCS (2–10 equivalents), I_2:HIO_3 (from 0.8 to excess equiv.) and Br_2 (from 0.8 to excess equivalents) were used for the synthesis of

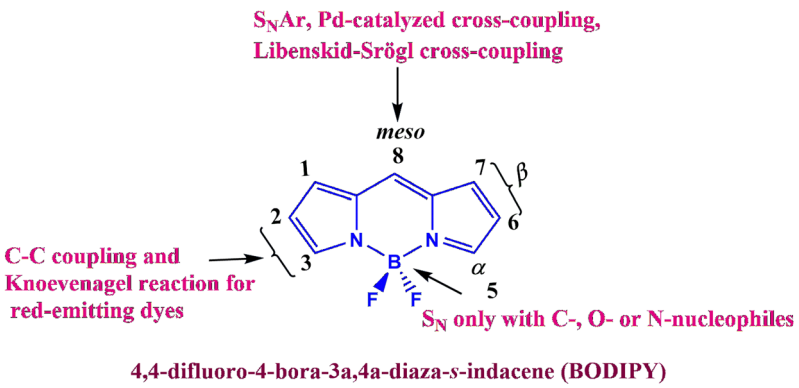

Fig. 2 Schematic representation of the structural modifications and chemical reactions of the BODIPY dye.

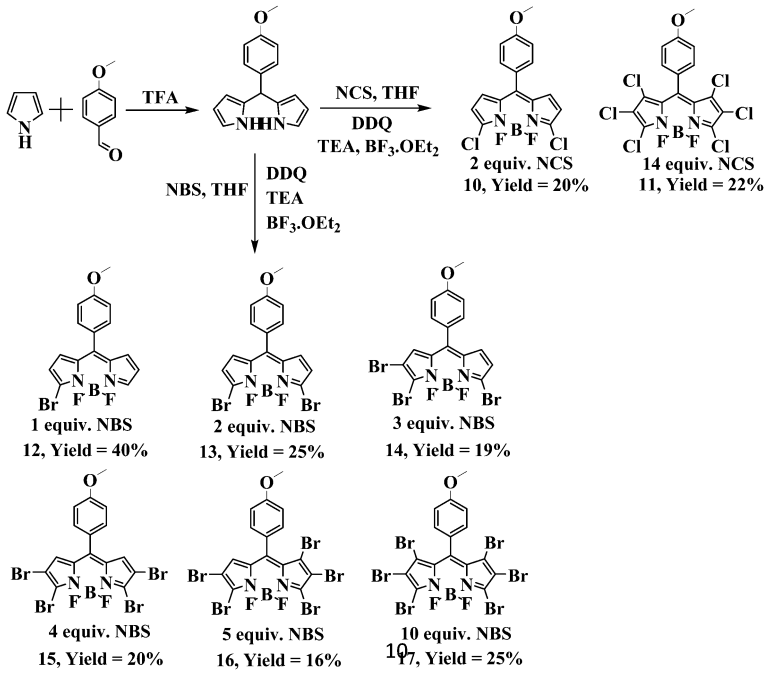

Scheme 8 Synthesis of halogenated BODIPYs **10–17**.

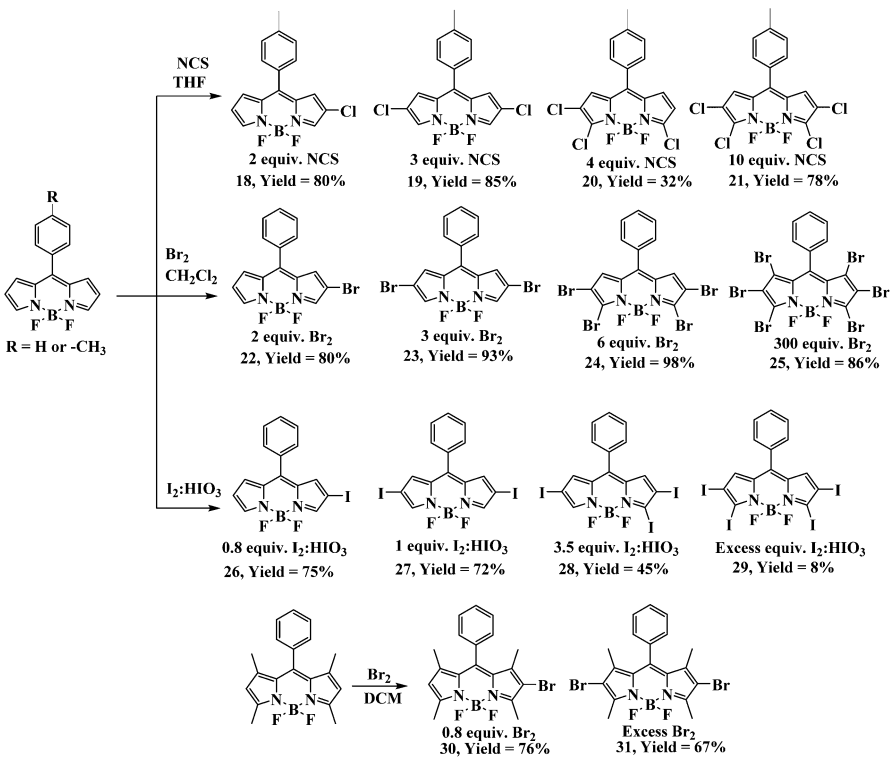

Scheme 9 Synthesis of chloro-, bromo- and iodo-substituted BODIPYs **18–31**.

β-halogenated BODIPYs **18–29** in 8–98% yields (Scheme 9). Methyl-substituted BODIPY reacts with 0.8 to excess equivalents of bromine, resulting in β-mono- and β-dibrominated BODIPYs **30** and **31** in 76% and 67% yield, respectively. The methyl-substituted BODIPY was used to avoid excess bromination.[78,79]

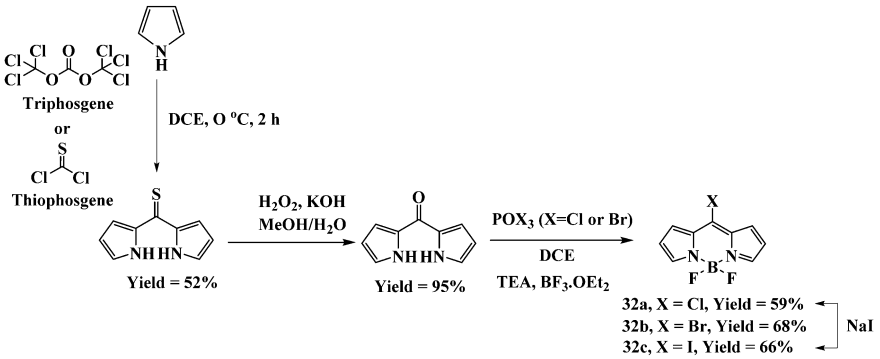

Scheme 10 Synthetic route for the 8-halo-BODIPY **32a–32c**.

1.3.1.3. Halogenation reaction at the meso-position of BODIPY. Dehaen *et al.* reported the synthesis of 8-chloro/8-bromo BODIPYs using phosphorus oxychloride ($POCl_3$)/phosphoryl bromide ($POBr_3$), respectively, followed by complexation with $BF_3{\cdot}OEt_2$.[80] The 8-chloro group can be replaced with the 8-iodo group using sodium iodide (NaI), which resulted in 8-iodo-BODIPY **32c** in 66% yield (Scheme 10). 8-Chloro-BODIPY was synthesized from the dipyrryl ketone. The dipyrryl ketone was obtained from the reaction of pyrrole and triphosgene or thiophosgene.[81] The dipyrryl thione, upon further reaction with H_2O_2, gives dipyrryl ketone. The dipyrryl ketone, upon further treatment with POX_3 (X = Cl or Br) followed by a complexation reaction with TEA and $BF_3{\cdot}OEt_2$, resulted in 8-halo-BODIPY **32a–32b** in 59% and 68% yield, respectively (Scheme 10).[46,80]

1.3.2. Incorporation of S, N and O at the *meso*-position of BODIPY. The 8-halo BODIPY derivatives are highly fluorescent and have been used as starting materials for synthesizing BODIPYs **33–41** *via* aromatic nucleophilic substitution reactions (Scheme 11). The chloro substituent is an excellent leaving group in the S_NAr reaction and exhibits high reactivity compared with the Br and I groups. 8-Chloro-BODIPY undergoes the S_NAr reaction to introduce S, N and O atoms at the *meso*-position using a suitable nucleophile and base (Scheme 11). BODIPYs **34**, **35** and **37** show absorption bands

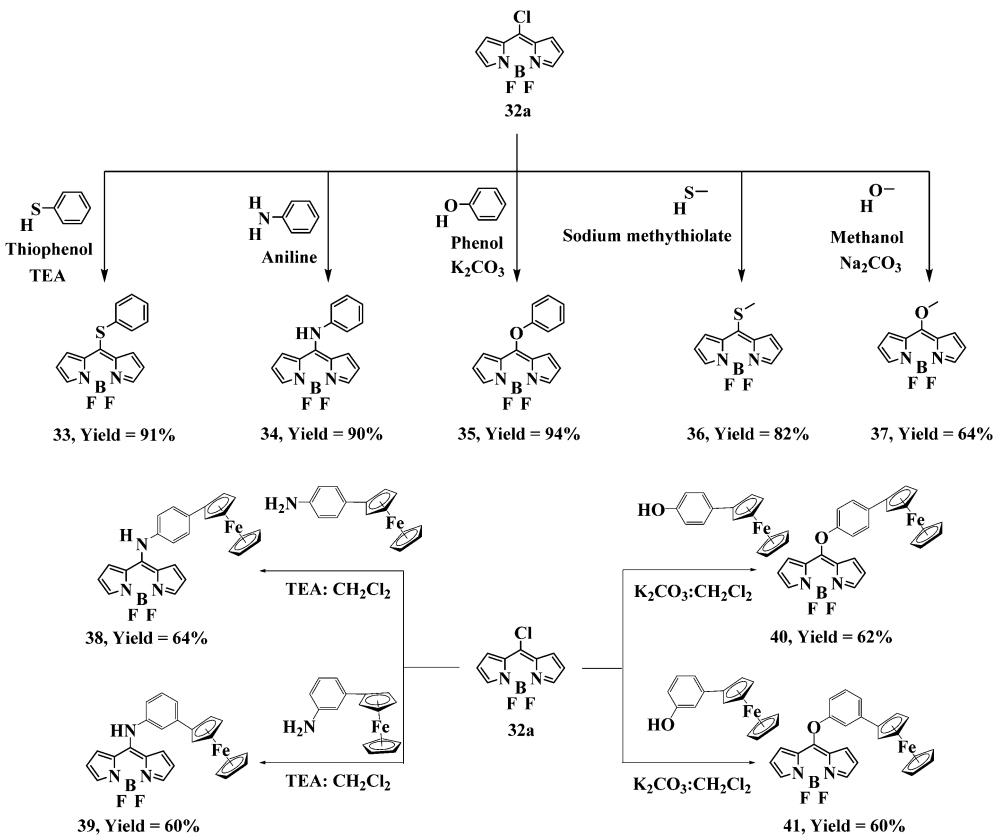

Scheme 11 Synthesis of *meso*-heteroatom-substituted BODIPYs **33–41**.

at 413 nm, 456 nm and 443 nm and emission bands at 420 nm, 495 nm and 486 nm, respectively. BODIPYs **35** and **37** exhibit high fluorescence quantum yield values, whereas the 8-N- and 8-S-substituted BODIPYs **33**, **34** and **36** are non-fluorescent. The BODIPY dye with an 8-N or 8-O substituent exhibited a blueshift in the absorption and emission bands compared with the unsubstituted BODIPY.[80]

Misra *et al.* investigated a series of O- and N-connected ferrocenyl BODIPYs **38–41** through the nucleophilic aromatic substitution (S_NAr) reaction using 8-chloro-BODIPY and ferrocenyl phenols/anilines (Scheme 11). BODIPYs **38** and **39** were synthesized by reacting 8-chloro-BODIPY with *para*- and *meta*-ferrocenyl aniline, respectively, whereas BODIPYs **40** and **41** were synthesized by reacting 8-chloro-BODIPY with *para*- and *meta*-ferrocenyl phenols, respectively. The absorption spectra of the nitrogen atom-linked BODIPYs **38** and **39** exhibited an 80 nm blueshift compared with 8-chloro-BODIPY, which exhibits a strong ($S_0 \rightarrow S_1$) absorption band at 503 nm. The oxygen-atom-linked BODIPYs **40** and **41** exhibit a 50 nm blueshift compared with 8-chloro-BODIPY. Overall, BODIPYs **38–41** exhibit absorption bands at 418 nm, 419 nm, 455 nm and 455 nm, respectively. The donor–acceptor BODIPYs **38–41** have oxidation potentials of 0.06 V, 1.06 V; 0.03 V, 1.12 V; 0.06 V, 1.07 V; and 0.10 V, 1.12 V, and reduction potentials of −1.19 V, −1.39 V; −1.21 V, −1.39 V; −1.14 V, −1.25 V; and −1.24 V, −1.28 V, respectively. The two reduction potentials are attributed to the BODIPY unit, and the two oxidation potentials correspond to oxidation of the ferrocenyl and BODIPY units. The BODIPYs **38–41** exhibited high thermal stability with decomposition temperatures at 300 °C, 309 °C, 264 °C and 254 °C, respectively.[33]

1.3.3. Vilsmeier–Haack formylation reactions of BODIPY. The α-mono- and α-diformylated BODIPYs were prepared using phosphorus oxychloride ($POCl_3$) and dimethylformamide (DMF), followed by DDQ for oxidation of the dipyrromethane intermediate (Scheme 12). After complete oxidation, the mixture was treated with TEA and $BF_3{\cdot}OEt_2$ for complexation, which results in the α-mono- and α-diformylated BODIPYs **42** and **43** in 15% and 26% yields, respectively. The β-mono- and β-diformylated BODIPYs **44** (yield = 68%) and **45** (yield = 82%) were synthesized after the formation of BODIPY using the Vilsmeier reagent (Scheme 12). BODIPYs **42–45** showed a characteristic absorption ($S_0 \rightarrow S_1$ (π–π^*)) transition at 540–550 nm. In addition, formylated BODIPYs **42–45** showed weak fluorescence because of the electron-rich *meso*-aryl group which is associated with photoinduced electron transfer with the BODIPY.[82,83]

1.3.4. Knoevenagel condensation reactions of BODIPY. Zang *et al.* reported the design and synthesis of carbazole-based BODIPY derivatives through the Knoevenagel condensation reaction for solar cell applications. The methyl-substituted BODIPY reacts with aldehyde groups in the presence of piperidine, acetic acid and toluene under reflux conditions (Dean–Stark apparatus). The mono-, di- and tetra-vinyl-substituted BODIPYs **46–48** were synthesized using 1.0, 3.0 and 6 equivalents of carbazole aldehyde (Ar), which resulted in yields of 37%, 79%, and 13%, respectively (Scheme 13). BODIPYs **46–48** show an absorption band at 590 nm, 674 nm, 728 nm, and an emission band at 609 nm, 692 nm and 755 nm, respectively. The fluorescence quantum yield of BODIPYs **46–48** is 0.69, 0.98 and 0.42, respectively. The frontier molecular orbitals calculated from the cyclic voltammetry of BODIPYs **46–48** have HOMO energy levels at −5.36 eV, −5.34 eV and −5.34 eV, and LUMO energy levels at −3.47 eV, −3.52 eV and −3.66 eV, respectively. The electrochemical bandgap values for BODIPYs **46–48**, estimated from the HOMO and LUMO values, are 1.89 eV, 1.82 eV and 1.68 eV, respectively. The decomposition temperatures for BODIPYs **46–48** were found to be at 346 °C, 372 °C and 305 °C, respectively. The Knoevenagel condensation reaction can be used to synthesize highly conjugated BODIPY dyes.[84] Obondi *et al.* reported a set of donor–acceptor-based

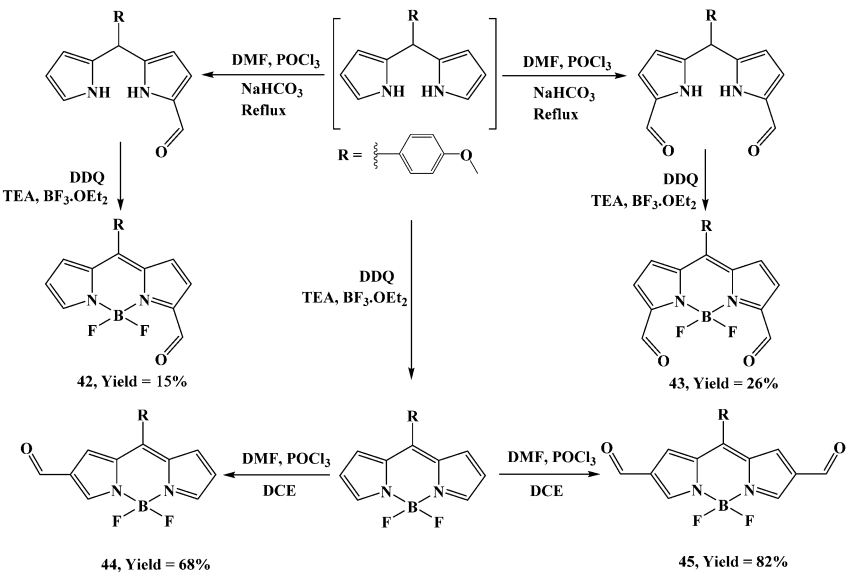

Scheme 12 Synthesis of mono- and diformylated BODIPYs substituted at the α- and β-positions (**42–45**).

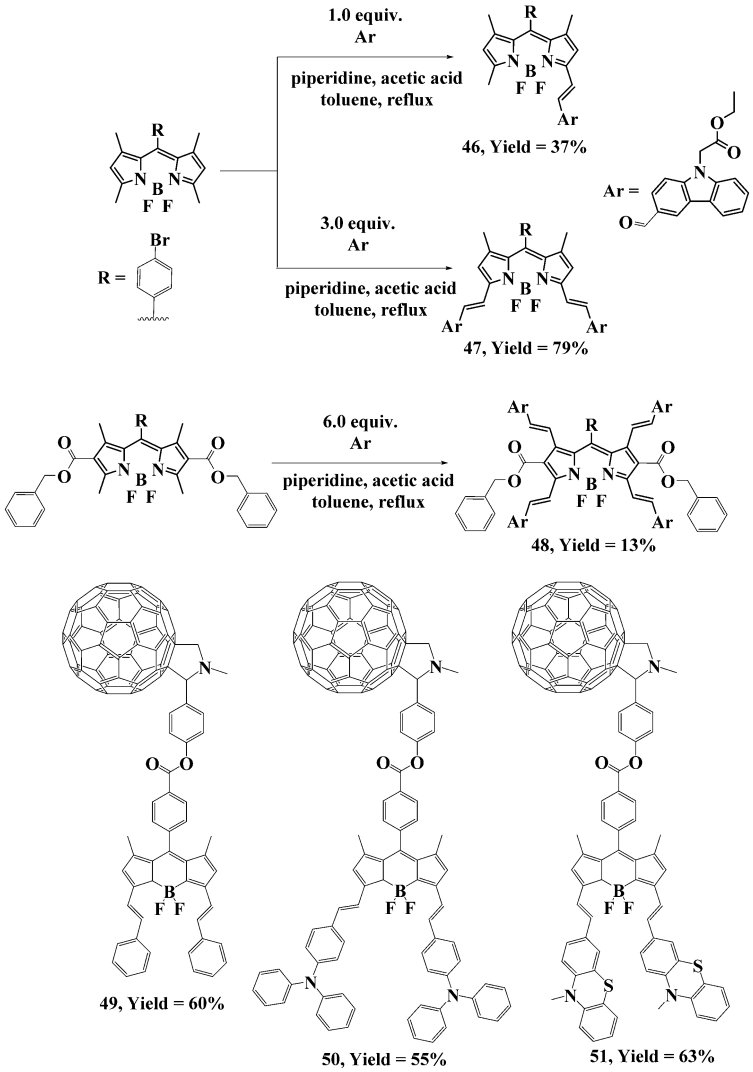

Scheme 13 Synthesis and molecular structures of BODIPYs **46–48** and **49–51**.

BODIPYs **49–51** in which the BODIPY unit is connected to two vinyl linkers that carry phenyl, triphenylamine and phenothiazine units, respectively (Scheme 13). The fulleropyrrolidine group acts as an electron acceptor at the *meso*-position of BODIPYs **49–51**. The BODIPYs **49–51** exhibit absorption and emission bands in the 300–850 nm region. The absorption spectra of BODIPYs **49–51** show a characteristic sharp peak of the fulleropyrrolidine moiety at 432 nm. BODIPYs **49–51** exhibit absorption peaks at 634 nm, 676 nm and 702 nm, and fluorescence peaks at 652 nm, 763 nm and 709 nm, respectively; in addition, BODIPYs **49–51** show fluorescence quantum yield values of 0.114, 0.07, <0.01, respectively. BODIPYs **49–51** exhibit oxidation potentials at 0.52 eV, 0.20 eV and 0.39 eV, and reduction potentials at −1.00 eV, −1.27 eV; −1.01 eV, −1.36 eV; and −1.00 eV, −1.31 eV, respectively. The triphenylamine- and phenothiazine-substituted BODIPYs **50** and **51** cover the spectrum range of 300–780 nm.[85]

1.3.5. Cross-coupling reactions of BODIPYs. Generally, cross-coupling reactions are used to synthesize BODIPY-based donor–acceptor chromophores. Halogen-substituted BODIPYs undergo Pd-catalyzed cross-coupling reactions such as the Sonogashira, Suzuki, Heck and Stille cross-coupling reactions.

1.3.5.1. Sonogashira cross-coupling reactions. Shinde *et al.* reported donor–acceptor BODIPYs, which were synthesized *via* the palladium-catalyzed Sonogashira cross-coupling reaction, and investigated their photophysical and redox properties. The precursors α-bromo-, β-iodo- and 8-chloro-BODIPY react with 1-ethynyl-4-(ethynylferrocene)benzene (1.0 equiv.) in the presence of the Pd-catalyst, which gives α-, β- and *meso*-ferrocenyl-substituted BODIPYs **52–54** in 83–85% yield (Scheme 14). BODIPYs **52–54** show absorption maxima at 568 nm, 545 nm and 550 nm, and emission maxima at 580 nm, 608 nm and 568 nm, respectively. The highest bathochromic shift was observed for BODIPY **52** compared with BODIPYs **53** and **54**. Electrochemical studies showed that BODIPYs **52–54** exhibit oxidation waves at 1.13 V, 0.97 V; 0.11 V, 1.03 V and 0.14 V, 1.04 V, and reduction waves at −1.16 V,

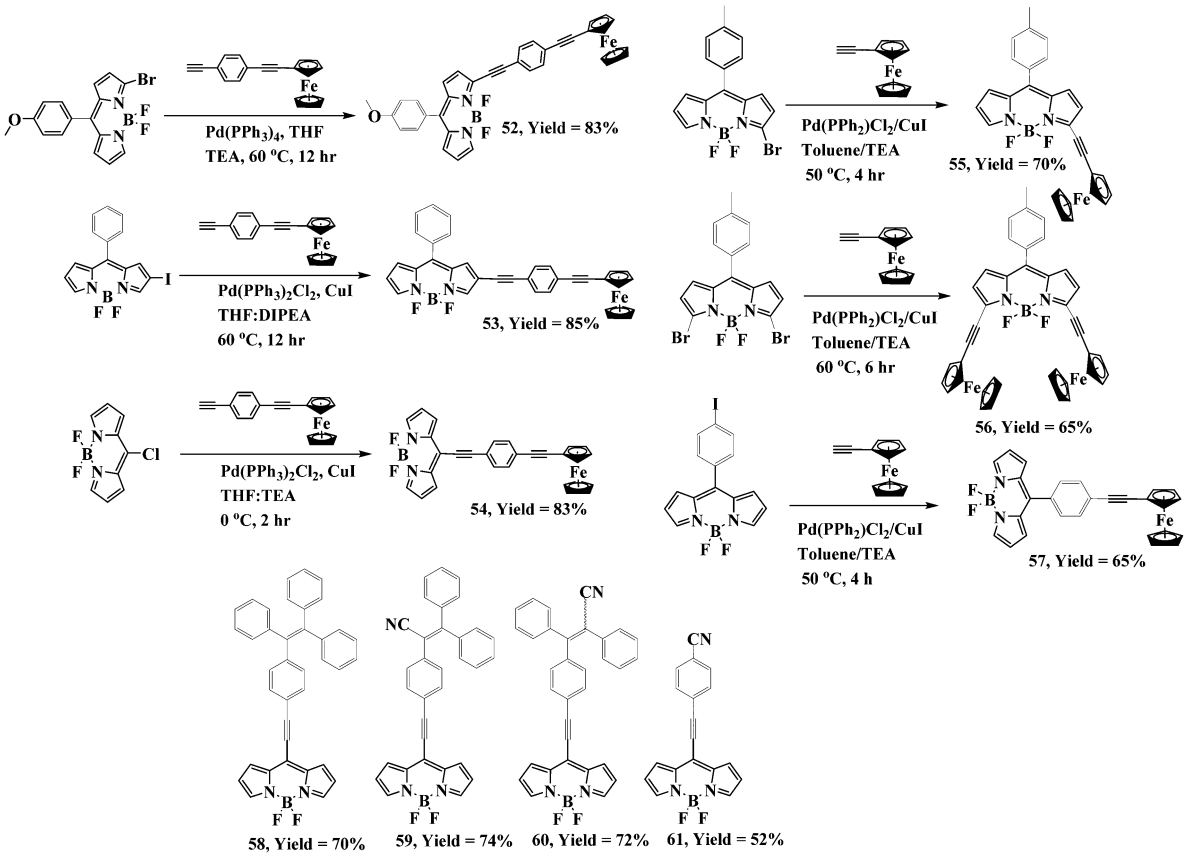

Scheme 14 Synthesis and molecular structures of the α-, β- and *meso*-substituted BODIPYs **52–61**.

−1.09 V and −0.97 V, respectively. Incorporating the ferrocene unit in BODIPYs **52–54** revealed that the oxidation values were anodically shifted by 0.11–0.14 V compared with pristine ferrocene oxidation.[86] Ravikanth and co-workers have reported BODIPY-ferrocene derivatives **55–57** in which either one or two ferrocenyl units are linked through an ethynyl group at the α- or *meso*-position of the BODIPY unit (Scheme 14). BODIPYs **55–57** exhibit absorption bands at 531 nm, 631 nm; 558 nm, 680 nm; and 505 nm, respectively. Absorption studies revealed that BODIPYs **55** and **56** show an ICT band in the UV-visible region due to strong conjugation between donor ferrocene and BODIPY. The CT band was not observed for BODIPY **57**, in which the ferrocene unit is attached to the *meso*-phenyl group of BODIPY, and shows less effective conjugation between ferrocene and BODIPY compared with BODIPYs **55** and **56**. BODIPYs **55–57** are non-fluorescent in nature due to the fast photo-induced electron transfer from the donor ferrocene to the acceptor BODIPY. Generally, BODIPY exhibits a single oxidation and single reduction wave due to the formation of the mono-cation and mono-anion, respectively. In BODIPYs **55–57**, the BODIPY moiety exhibits a single irreversible oxidation wave in the range of 1.30–1.50 V and a single reversible reduction wave in the region from −0.70 V to −0.80 V, although BODIPY **57** shows only one reduction. BODIPYs **55–57** show reversible oxidation in the 0.64–0.74 V region, which is attributed to the oxidation of ferrocene to the ferrocenium ion.[87] Dhokale *et al.* reported the synthesis of BODIPYs **58–61** using the palladium-catalyzed Sonogashira cross-coupling reaction (Scheme 14). BODIPYs **59** and **60** exhibit red-shifted absorption and emission as well as high fluorescence quantum yield values compared with BODIPY **58**. BODIPYs **58–61** exhibit absorption bands at 468 nm, 543 nm; 435 nm, 546 nm; 428 nm, 546 nm; and 552 nm, whereas the emission bands were observed at 561 nm, 731 nm; 564 nm; 564 nm; and 571 nm, respectively. The presence of the electron-withdrawing group at the *meso*-position of BODIPY shows a blueshift in both the absorption and emission spectra and lowers the quantum yield.[52]

1.3.5.2. Suzuki cross-coupling reactions. Ravikanth *et al.* synthesized a set of mono-, and diphenyl-substituted BODIPYs (**62** and **63**) through the Pd-catalyzed Suzuki cross-coupling reaction and investigated their optical and redox properties. The α- and β-bromo-BODIPY derivatives were reacted with controlled equivalents of phenylboronic acid in the presence of the Pd-catalyst, Na_2CO_3, and toluene : THF : H_2O (6 : 3 : 1) under reflux conditions, resulting in the mono- and diphenyl-substituted BODIPYs **62** and **63** in 85% and 87% yield, respectively (Scheme 15). The phenyl-substituted BODIPYs **62** and **63** exhibit absorption bands in the 500–600 nm region,

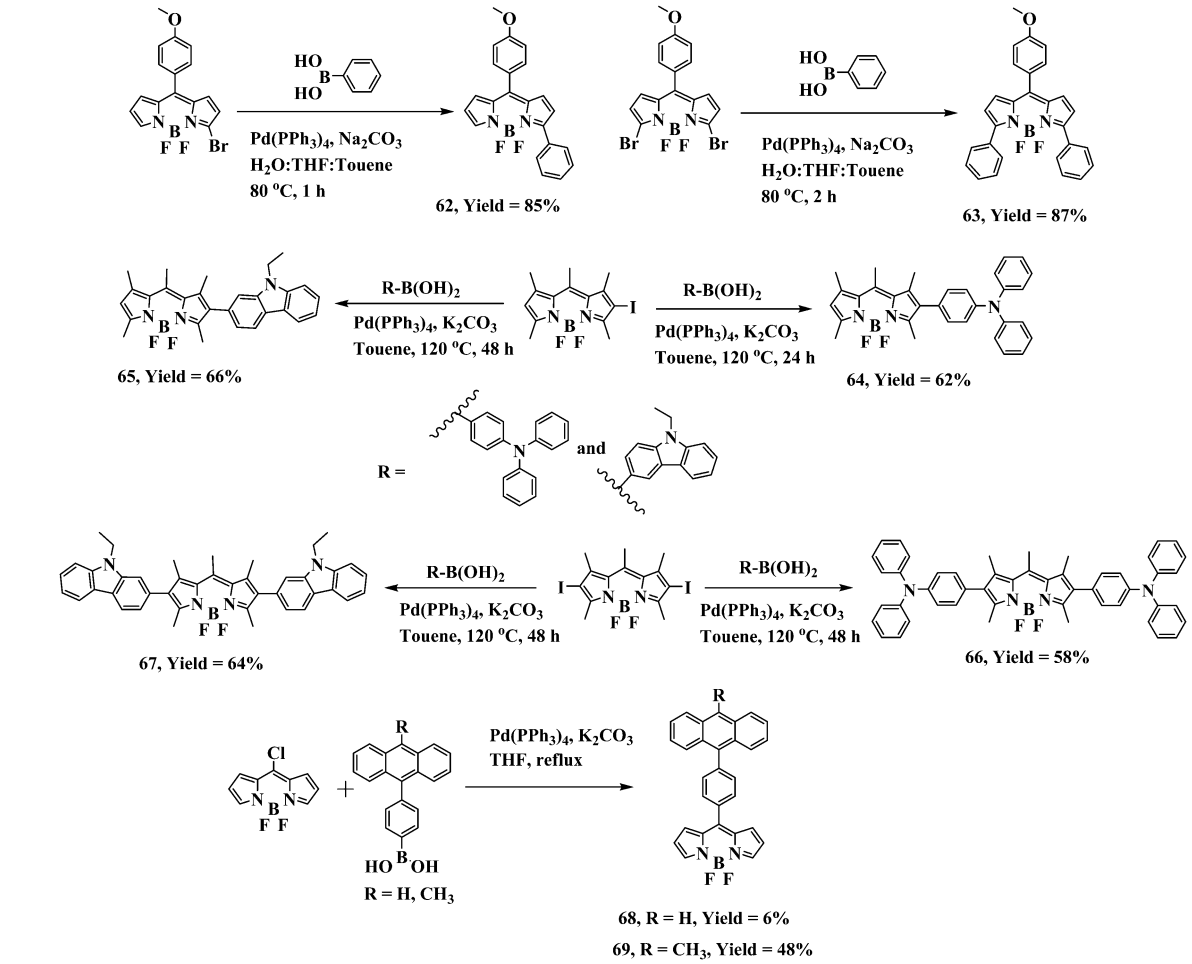

Scheme 15 Synthesis of the BODIPYs **62–69**.

corresponding to the $S_0 \rightarrow S_1$ transition, and a vibronic transition at about 400 nm, corresponding the $S_0 \rightarrow S_2$ transition. BODIPYs **62** and **63** exhibit oxidation potential values at 1.46 V and 1.33 V, and reduction potential values at −0.83 V and −0.84 V, respectively.[88] Recently, Wanwong *et al.* reported the series of donor–acceptor BODIPYs **64–67** using the Pd-catalyzed Suzuki cross-coupling reaction in which triphenylamine and carbazole act as donor groups and BODIPY acts as the acceptor (Scheme 15). BODIPYs **64–67** exhibited two strong absorption bands in the range of 269–307 nm and 511–531 nm with high extinction coefficients (10^4 M^{-1} cm^{-1}). The absorption maxima of BODIPYs **66** and **67** are redshifted by 25 nm and 20 nm compared with BODIPYs **64** and **65**, respectively. The optical bandgap values of BODIPYs **64–67** were 2.05 eV, 2.07 eV, 1.98 eV and 2.00 eV, respectively. Triphenylamine and carbazole were used as the donor groups, which easily undergo oxidation to radical cations and can be employed in various optoelectronic applications. The redox properties of BODIPYs **64–67** exhibit oxidation waves at 0.39 V, 0.45 V, 0.23 V and 0.37 V, and these are attributed to the HOMO energy levels of −5.03 eV, −5.10 eV, −4.92 eV and −5.06 eV, respectively.[89] Kim *et al.* have reported the 8-chloro-BODIPY-based chromophores **68** and **69** *via* the Suzuki cross-coupling reaction, which are useful for singlet oxygen generation ($^1O_2$). The 8-chloro-BODIPY was reacted with anthraphenyleneboronic acid in the presence of a palladium catalyst, potassium carbonate and THF solvent under reflux conditions, resulting in orange-colored anthracene-based D–A BODIPYs **68** and **69** (Scheme 15). BODIPYs **68** and **69** exhibit an absorption band at 498 nm and emission bands at 517 nm and 519 nm, respectively, in MeOH solvent.[90]

1.3.5.3. Stille cross-coupling reaction. In 2014, Ziessel *et al.* synthesized 3,5-substituted thiophene–benzothiadiazole–thiophene-functionalized BODIPY **70** *via* the Stille cross-coupling reaction. The α-dibromo-BODIPY derivative reacts with stannyl thiophene–benzothiadiazole–thiophene in the presence of a Pd-catalyst and tri(*o*-tolyl)-phosphine using toluene under reflux conditions, which resulted in the purple-colored α-dithiophene–benzothiadiazole–thiophene-substituted BODIPY **70** in 83% yield (Scheme 16). BODIPY **70** absorbs at up to 800 nm in solution and at up to 900 as a thin film. The absorption spectrum of BODIPY **70** shows three peaks: the thiophene unit shows a peak at 320 nm that overlaps with the $S_0 \rightarrow S_2$ transition of the BODIPY unit and a CT peak, which was

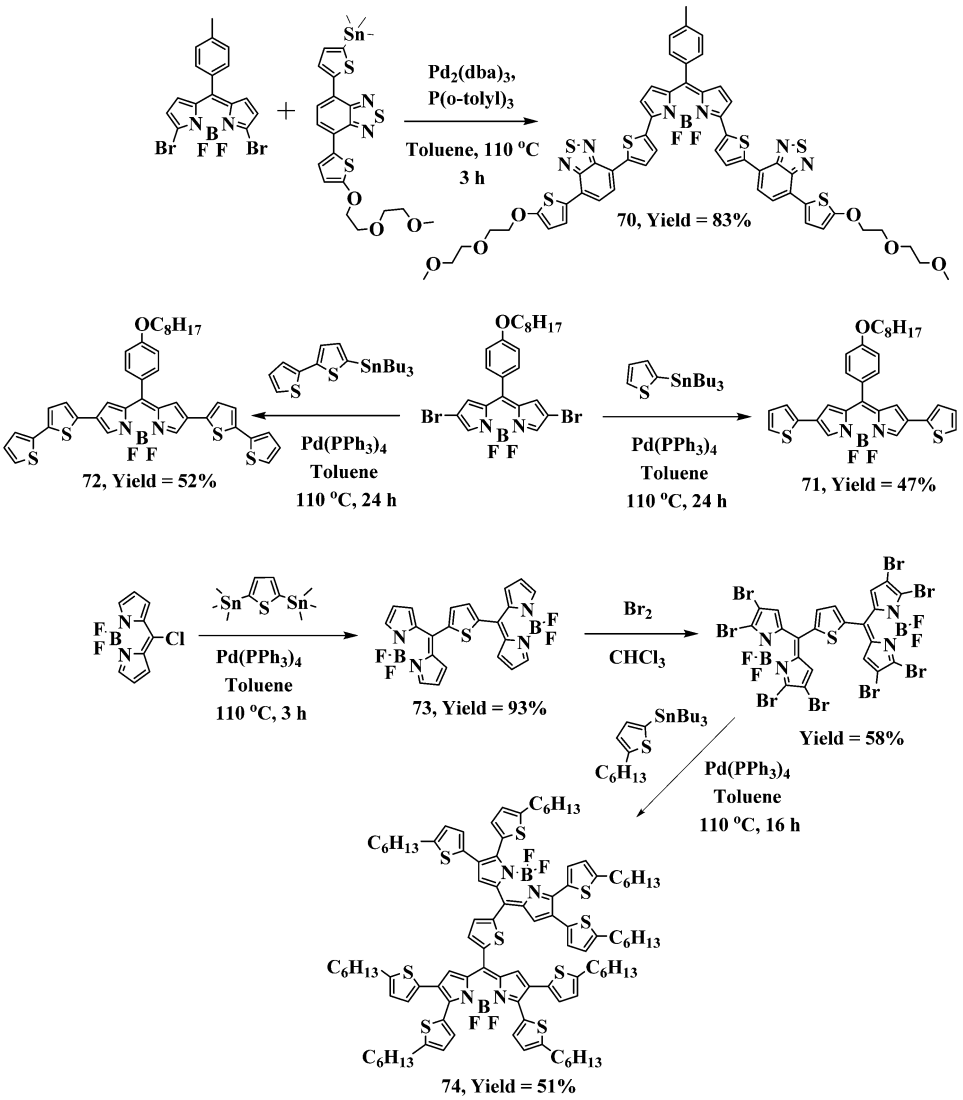

Scheme 16 Synthesis of thiophene-functionalized BODIPYs **70–74**.

observed at 537 nm. The intense peak at 737 nm was assigned to the $S_0 \rightarrow S_1$ (π–π^*) transition of BODIPY.[91]

Yang *et al.* reported the D–A–D-based BODIPYs **71** and **72**, which were synthesized *via* the Stille cross-coupling reaction for organic solar cells (OSCs). The β-dibromo-BODIPY derivative reacts with tributyl(thiophen-2-yl)stannane and [2,2′-bithiophen]-5-yltributylstannane in the presence of a Pd-catalyst using toluene as the solvent at 110 °C for 24 h, which resulted in BODIPYs **71** and **72**, respectively (Scheme 16). The decomposition temperature of BODIPYs **71** and **72** is at 221 °C and 305 °C, respectively. BODIPYs **71** and **72** show three absorption bands: the first absorption band in the 280–350 nm region is due to the π–π^* transition of the electron donors thiophene and bithiophene; the second band at 350–500 nm belongs to the π–π^* transition of BODIPY; the third absorption band in the 500–800 nm region is attributed to the π–π^* transition and ICT. The power conversion efficiency (η) values for organic solar cells (OSCs) based on BODIPYs/$PC_{61}BM$ (1 : 0.5, w/w) are 1.49% for BODIPY **71** and 2.15% for BODIPY **72**.[92] Leclerc *et al.* synthesized BODIPYs **73** and **74** through the Stille cross-coupling reaction. The reaction of the 8-chloro- and the octabromo-substituted BODIPY derivatives with bis(trimethylstannyl)thiophene and tributyl(5-hexylthiophene2-yl)stannane using $Pd(PPh_3)_4$, respectively, in toluene under reflux conditions for 3 h and 16 h resulted in BODIPYs **73** and **74** in 93% and 51% yields, respectively (Scheme 16).

BODIPYs **73** and **74** exhibit an absorption maxima at 520 nm, 486 nm, and at 697 nm, 706 nm, respectively. For each, the absorption band in the higher wavelength region is due to the $S_0 \rightarrow S_1$ transition, and the second band is attributed to intramolecular charge transfer between the thiophene donor and the acceptor BODIPY moiety. The dimerization methodology of polycyclic aromatic units is a powerful strategy for the synthesis of BODIPY-based materials for organic solar cell applications.[93]

1.3.5.4. Heck cross-coupling reaction. In 2021, Knight *et al.* reported BODIPY derivative **75**, which was synthesized *via* a Pd-catalyzed Heck coupling reaction. The α-dibromo-BODIPY

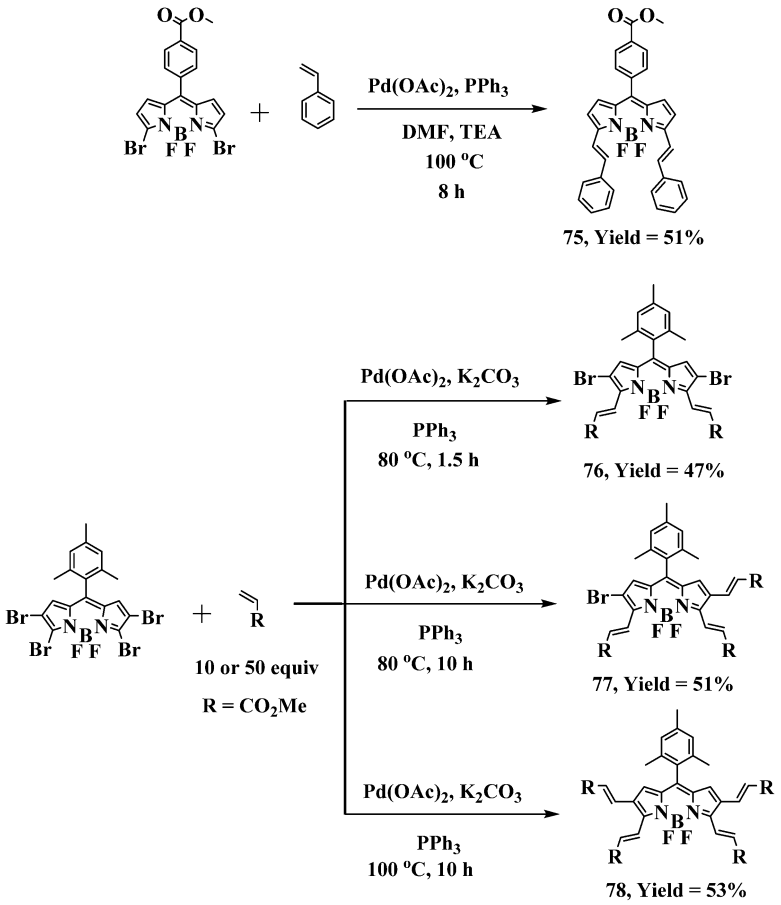

Scheme 17 Synthesis of phenyl-substituted BODIPYs **75–78**.

derivative was reacted with styrene, $Pd(OAc)_2$, PPh_3, DMF and TEA to give the 3,5-distyrene-substituted BODIPY **75** in 51% yield (Scheme 17).[94] Hao *et al.* have reported the regioselective and stepwise synthesis of BODIPYs **76–78** using the palladium(II)-catalyzed Heck cross-coupling reaction. The tetra-substituted bromo-BODIPY derivative reacts with 10–50 equivalents of methyl acrylate, $Pd(OAc)_2$, PPh_3, and K_2CO_3 at different temperatures, resulting in the alkenyl-substituted BODIPYs **76–78** in 47%, 53% and 51% yield, respectively (Scheme 17). The respective BODIPYs **76–78** exhibit an absorption band at 612 nm, 622 nm and 634 nm and an emission band at 628 nm, 655 nm and 669 nm. The Stokes shift of BODIPYs **76–78** is 416 cm^{-1}, 810 cm^{-1}, and 825 cm^{-1}, respectively. BODIPYs **76** and **77** (*i.e.*, BODIPYs with bromo substituents at the 2- and 6-positions) show efficient singlet oxygen ($^1O_2$) generation due to the heavy atom effect.[95]

1.3.6. C–H amination of BODIPY. In 2018, You *et al.* reported a series of highly efficient BODIPYs **79–83** using Ag-mediated direct C–H amination for the screening of ER (endoplasmic reticulum)-targeting reagents. The C–H amination of BODIPY was carried out with amines and using 4.0 equivalents of AgOAc as the oxidant under a nitrogen atmosphere. The best result was obtained in DMSO (dimethyl sulfoxide) solvent at 80 °C for 12 h (Scheme 18). The BODIPYs with electron-withdrawing trifluoromethyl or cyano groups, or the electron-donating methyl group, on the *meso*-aryl group undergo a direct C–H amination reaction in high yields. The respective BODIPYs **79–83** show an absorption band at 571 nm, 545 nm, 564 nm, 561 nm, 487 nm, and an emission band at 587 nm, 576 nm, 636 nm, 592 nm, and 557 nm. Most of these π-conjugated BODIPYs emit green and yellow fluorescence. Cell-imaging experiments showed that BODIPYs **80** and **82**, which contain benzimidazole, have excellent ER-labelling capacities.[96]

1.3.7. Grignard reaction. Ziessel *et al.* synthesized the π-conjugated BODIPYs **84** and **85** based on substitution with the alkynylaryl residue at the boron center of the BODIPY. The use of 2.0 equivalents of the ethynyl-Grignard reagent enabled the substitution of both fluorine atoms with two ethynylpyrene groups using THF under reflux conditions (Scheme 19).

BODIPY **84** shows an absorption and emission band at 531 nm and 549 nm, respectively, in DCM. BODIPY **85** shows an absorption band at 709 nm and an emission band 750 nm in DCM solvent with a Stokes shift of 771 cm^{-1}.[97,98] Rousseau *et al.* reported the 5-hexyl-2,2-bithienyl-substituted BODIPY **86** for bulk heterojunction solar cell applications (Scheme 19). BODIPY **86** was synthesized using a Grignard reagent to replace the fluorine atoms with ethynyl residues, resulting in a 95% yield. BODIPY **86** shows an absorption band at 649 nm, an emission band at 661 nm and a fluorescence quantum yield of 0.63.[99] Rihn *et al.* reported the preparation of BODIPY **87** in

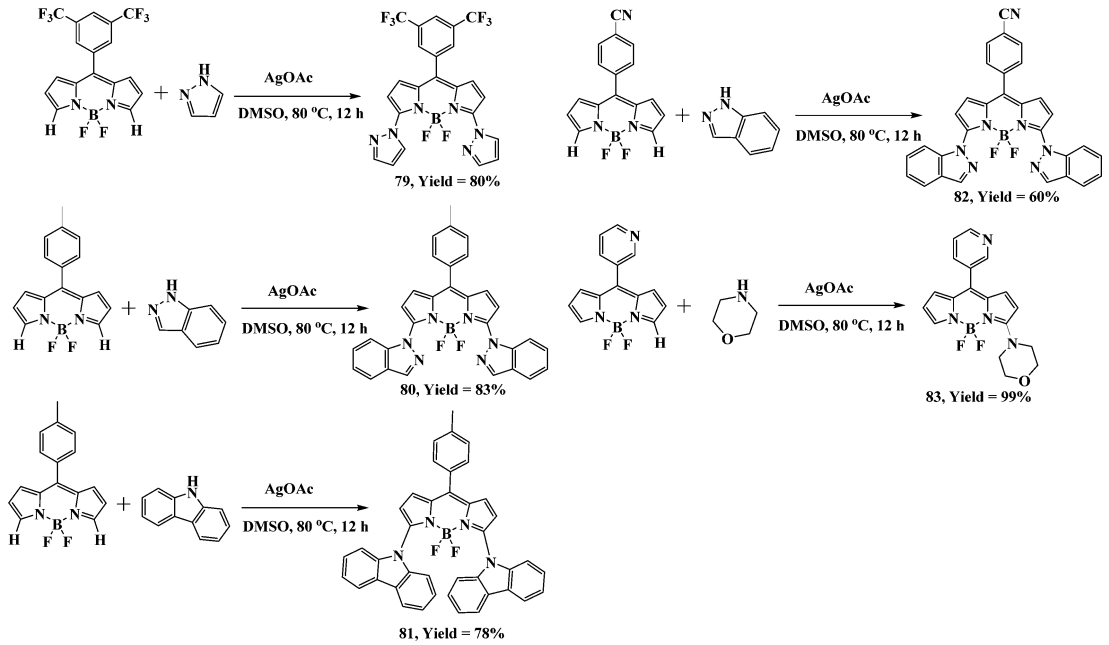

Scheme 18 Synthesis of α-mono- and -di-substituted BODIPYs **79–83** synthesized *via* C–H amination.

66% yield using an excess of ethynyl-Grignard reagent (Scheme 19). BODIPY **87** exhibits absorption bands at 360 nm and 520 nm, an emission band at 562 nm, and a fluorescence quantum yield of 0.70. Substitution at the boron center with 1-ethynylpyrene does not affect the emission properties. The pyrene unit shows two absorption bands, at 285 nm and 369 nm, which are assigned to the π–π* transition.[100]

1.4. Similar structures as BODIPY

1.4.1. BOIMPY dyes. BOIMPY (bis(borondifluoride)-8-imidazodipyrromethene) dyes are a new class of fluorophore with large π-conjugated skeletons that allow various functionalizations to extend the absorption band towards the NIR region. In 2021, Werz *et al.* reported the red-emitting BOIMPY (bis(borondifluoride)-8-imidazodipyrromethene) fluorophores **88** and **89**, which exhibit high fluorescence quantum yield values. The *meso*-position of the benzimidazole unit contains two BF_2 groups, which results a rigid and planar conjugated system. BOIMPY derivatives offer easy functionalization possibilities, such as nucleophilic fluorine substitution, Knoevenagel condensation and cross-coupling reactions, making them valuable fluorophores for optoelectronic applications. BOIMPYs **88** and **89** were synthesized through the reaction of benzimidazole-2-carboxylic acid, oxalyl chloride, and pyrrole, followed by DBU and $BF_3{\cdot}OEt_2$, in 39% and 31% yields, respectively (Fig. 3). BOIMPYs **88** and **89** show absorption and emission bands at 596 nm and 605 nm, and fluorescence quantum yields of 0.72 and 0.73, respectively.[101] Patalag *et al.* reported the highly fluorescent and photostable fluorophores BOIMPYs **90–93** *via* the Knoevenagel condensation reaction using substituted aldehydes (Fig. 3). The respective BOIMPYs **90–93** show an absorption band at 803 nm, 951 nm, 784 nm and 783 nm. Computational studies showed that the LUMO is partially delocalized outside the pyrrole unit, whereas the HOMO is located over the BOIMPY core.[102] Werz and co-workers have reported a series of red- and NIR-absorbing push–pull BOIMPYs (**94–96**; Fig. 3) and studied their photophysical, electrochemical and computational properties. The respective BOIMPYs **94–96** show an absorption band at 703 nm, 719 nm and 826 nm, and an emission band at 736 nm, 811 nm and 835 nm, with fluorescence quantum yield values of 0.13, 0.07 and 0.03. The absorption spectra reveal that the absorption band shifts towards a higher wavelength region upon increasing the donor strength, which follows the order **96** > **95** > **94**. The introduction of electron-donating thienyl and furyl groups significantly altered the HOMO and LUMO energies, suggesting that the BOIMPY motifs are useful candidates for molecular electronics or dye-sensitized solar cell (DSSC) applications.[103]

1.4.2. BOPHY dyes. Tetracoordinate BF_2 complexes occupy a privileged position among all the fluorophores due to their easy synthetic procedure, facile structural modifications, and good photochemical stability and photophysical properties. These properties have enabled BOPHY (bis(difluoroboron)-1,2-bis((1*H*-pyrrol-2-yl)methylene)hydrazine) dyes to be used in photoconductors as *in vitro* and *in vivo* imaging agents, electrochromic devices and many more. Ziegler and co-workers reported the new BOPHY fluorophore, which has a rigid planar structure that possesses C_{2h} symmetry.[104] The α-, β- and *meso*-positions of BOPHY can be functionalized to synthesize various donor–acceptor BOPHY derivatives. BOPHY has been synthesized *via* the reaction of pyrrole-2-carboxaldehyde and hydrazine, which results in a pyrrole-imine dimeric chelate, followed by complexation with $BF_3{\cdot}OEt_2$.[105] In 2018, Yu *et al.* reported the tetramethyl-substituted fluorescent BOPHY **97**, synthesized *via* the Knoevenagel condensation reaction with 10-methyl-10*H*-phenothiazine-3-carbaldehyde, which was used

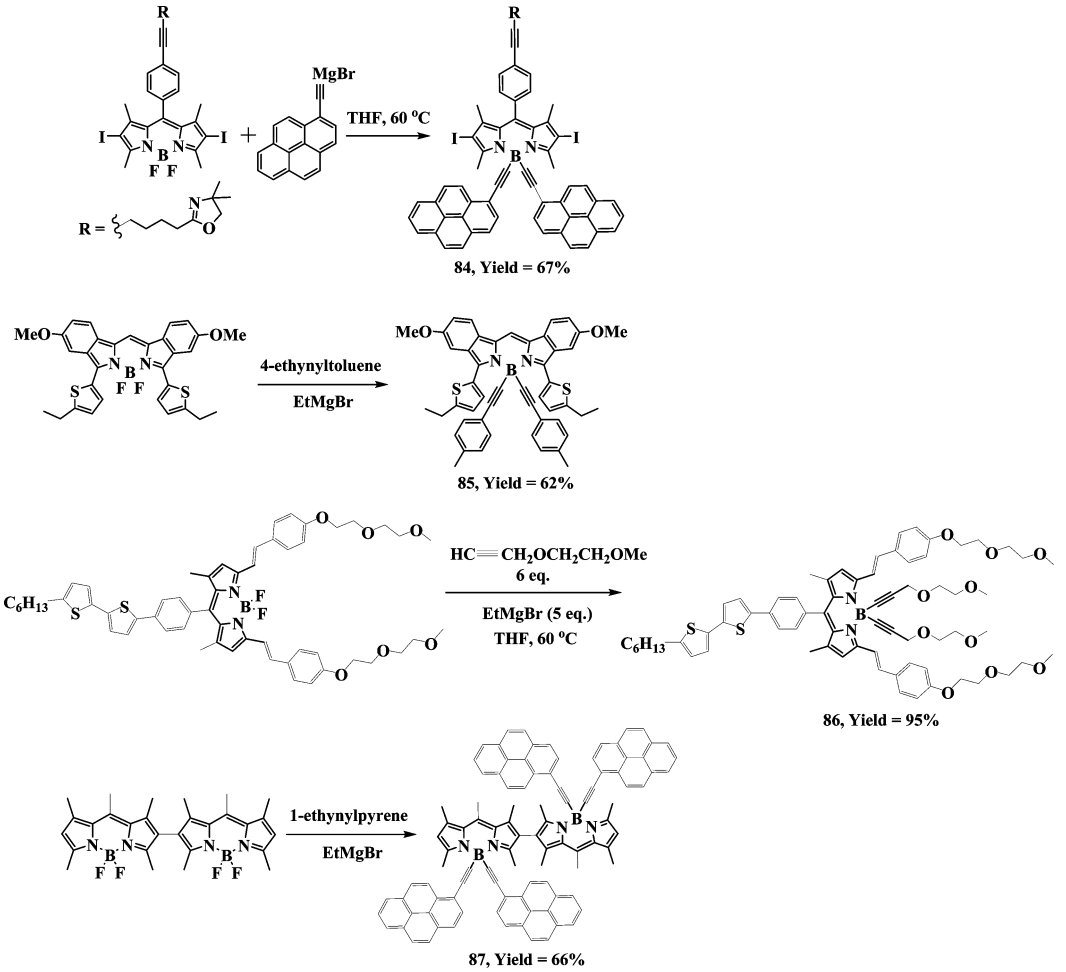

Scheme 19 Synthesis of BODIPYs **84–87** *via* the Grignard reaction.

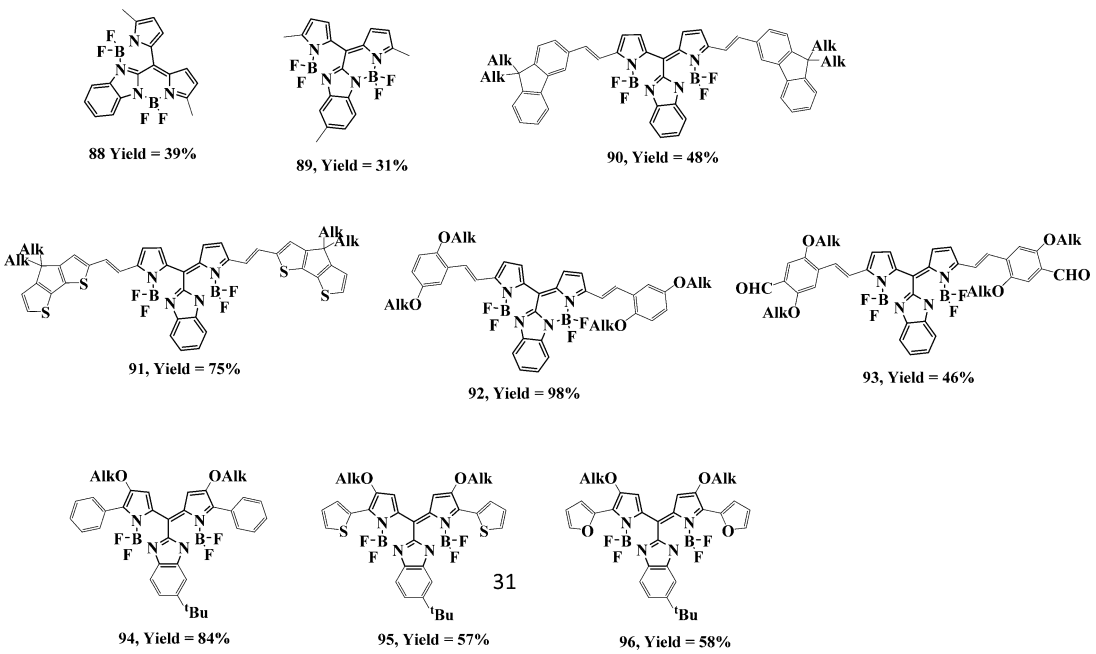

Fig. 3 Molecular structures of the red-emitting BOIMPYs **88–96**.

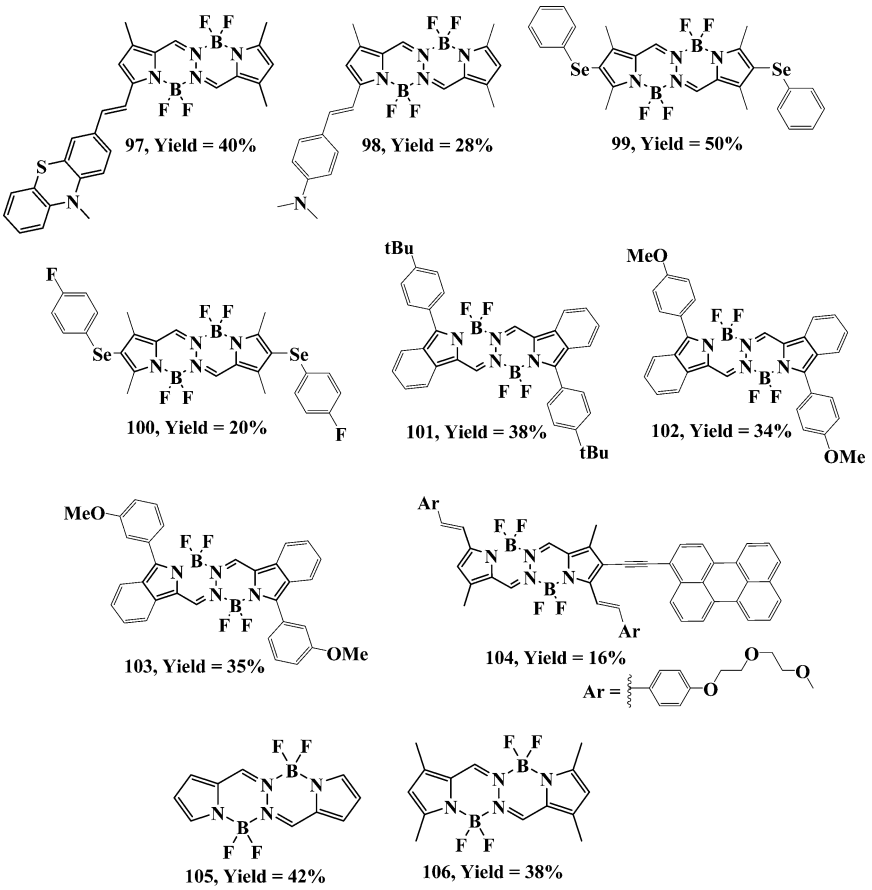

Fig. 4 Structures of the BOPHY-based derivatives **97–106**.

for Cu^{2+} ion sensing (Fig. 4). The Cu^{2+} ion was involved in the oxidation of the phenothiazine unit, inhibiting the ICT process from the donor to the acceptor, which results in strong fluorescence in solution.[106]

Xiao and co-workers reported the design and synthesis of mono-substituted BOPHY **98**, with the (*p*-dimethylamino)styryl group, *via* the Knoevenagel condensation reaction (Fig. 4). BOPHY **98** was non-emissive due to intramolecular charge transfer, and strong fluorescence was observed *via* protonation of the tertiary amine in BOPHY **98**. BOPHY **98** was used as a pH probe in biological applications.[107] Hasegawa *et al.* reported the synthesis of BOPHYs **99** and **100** by introducing the arylselenyl group at the 2 and 7 positions (Fig. 4). Direct C–Se bond formation facilitated intersystem crossing (ISC) to the triplet state, which is useful for triplet sensitizers. The photophysical properties of BOPHYs **99** and **100** were affected due to the presence of the heavy selenium atom. The respective BOPHYs **99** and **100** exhibit an absorption maximum at 459 nm and 482 nm, and an emission maximum at 519 nm and 517 nm.[108] Wang *et al.* reported fused BOPHYs **101–103** (Fig. 4) and explored their photophysical and electrochemical properties. BOPHYs **101–103** exhibit significant bathochromic shifts in absorption (up to 600 nm in solution) and emission (up to 648 nm in solution and 717 nm in the solid state), and high photochemical stability. The respective BOPHYs **101–103** exhibit absorption maxima at 423 nm, 571 nm and 563 nm, and emission bands at 468 nm, 614 nm and 602 nm in DCM solvent.[109] Ziessel and co-workers reported the design and synthesis of BOPHY **104** (Fig. 4) *via* the Knoevenagel reaction, which shows an absorption maximum above 625 nm. The perylene unit was linked to BOPHY using the Pd(0)-catalyzed cross-coupling reaction. BOPHY **104** is fluorescent, and intramolecular cascade energy transfer occurs from perylene to BOPHY, resulting in a high Stokes shift (>5100 cm^{-1}).[110] Nemykin and co-workers reported fluorescent BOPHYs **105** and **106** in 42% and 38% yield, respectively, from the coupling of pyrrole-2-carboxaldehyde with hydrazine and a complexation reaction with a boron complex. BOPHYs **105** and **106** exhibit absorption bands at 424 nm, 442 nm and 444 nm, 467 nm, with high fluorescence quantum yields of 0.95 and 0.92, respectively.[111]

1.4.3. Formazanate derivatives. Formazanates are a class of highly colored molecules that contain electron-rich nitrogen atoms, with the formula Ar–NH–N═CR–N═N–Ar. Their bright color has led to their extensive use as dyes, particularly in cell biology, where they are frequently used to quantify cell viability. Formazanate ligands are highly conjugated with excellent optoelectronic and redox properties. These properties can be tuned *via* structural modification of the formazanate unit. In 2021, Gilroy *et al.* reported the π-conjugated A–D–A-based

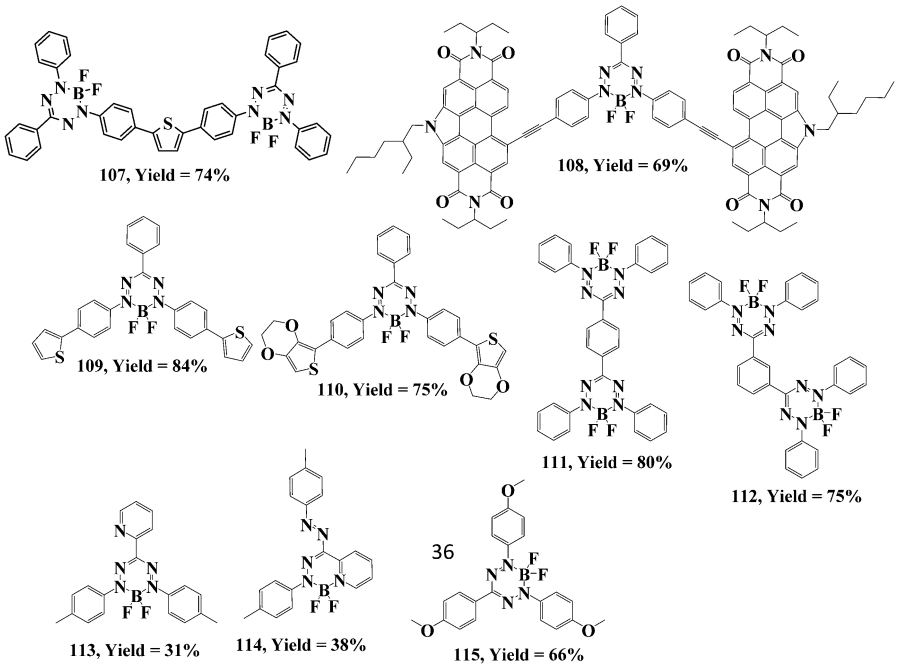

Fig. 5 Structures of formazanate derivatives **107–115**.

formazanate **107** (Fig. 5) and explored its optoelectronic properties. Formazanate **107** exhibits excellent photophysical and electrochemical properties, which can be tuned using an appropriate group at the *para*-position of the *N*-aryl rings of the formazanate. In addition, formazanate **107** shows an absorption band at 596 nm and a molar extinction coefficient of 52 400 M^{-1} cm^{-1}. The oxidation and reduction potentials of formazanate **107** were observed at 0.82 V, 1.07 V, and −1.96 V, −0.90 V, respectively. Formazanate derivatives show their applications in fluorescence cell-imaging, electrochemiluminescent materials and organic solar cells (OSC).[112] Koenig *et al.* reported the non-fullerene acceptor formazanate **108** (Fig. 5) that is end-capped with *N*-annulated perylene diimides. The electronic coupling between BF_2 formazanate and perylene diimides tuned the LUMO energy levels, resulting in a bathochromic shift in the absorption spectrum. In solution, BF_2 formazanate **108** shows a broad absorption between 450 and 750 nm, with a maximum absorption at 543 nm.[113] Kumar *et al.* reported the thiophene-capped BF_2 formazanates **109** and **110** using a Pd-catalyzed cross-coupling reaction (Fig. 5). Formazanates **109** and **110** possess a panchromatic absorption with a low HOMO–LUMO gap and are useful as light-harvesting organic materials. The absorption band of formazanates **109** and **110** was obtained at 570 nm and 606 nm, respectively. The ethylenedioxythiophenyl-substituted formazanate **110** exhibits a redshift compared with the thienophenyl-substituted formazanate **109** because of the donating nature of thiophene and extension of the π-conjugation.[114]

Barbon *et al.* reported the boron difluoride (BF_2) formazanate dimers **111** and **112** (Fig. 5) and investigated their photophysical and electrochemical properties. Dimer **112** exhibits bathochromically shifted absorption and emission bands compared with the monomer due to the increase in conjugation; both dimers **111** and **112** are non-emissive and exhibit high Stokes shifts (>110 nm). The dimers **111** and **112** show absorption bands at 509 nm and 523 nm and emission bands at 627 nm and 654 nm, respectively, in DCM solvent.[115] Gilroy and co-workers reported the flexidentate pyridine- and toluene-substituted formazanates **113** and **114**, respectively (Fig. 5). The coordination chemistry of both adducts was studied *via* their reaction with nickel(II) bromide [$NiBr_2(CH_3CN)_2$], and triflate [$Ni(OTf)_2$] salts. The photophysical properties of the formazanate adduct indicate a redshifted absorption band with low reduction potentials when coordinated with nickel(II) ions. The electronic and physical properties of formazanates **113** and **114** can be tuned through protonation.[116] Hesari *et al.* reported the boron difluoride formazanate **115** (Fig. 5) that contains *p*-methoxyphenyl units and explored the redox and electrogenerated chemiluminescence (ECL) properties. Formazanate **115** exhibits two quasi-reversible oxidation peaks at 1.00 V and 1.30 V, and two reversible reduction peaks at −0.67 V and −1.80 V.[117]

2. Applications of BODIPY chromophores

2.1. Dye-sensitized solar cells (DSSCs)

Global energy consumption has increased significantly in recent years due to population growth in developing nations. Throughout the world, fossil fuels, which include natural gas, crude oil and coal, account for about 80% of all energy consumption. Thus, DSSCs have attracted the attention of the scientific community due to the increasing demand for energy

and their low cost, ease of production and environmental friendliness. In 1991, Grätzel *et al.* presented a study on DSSCs, which have become cutting-edge technology in photovoltaics due to their low cost of production and excellent power conversion efficiency (η) values.[118] DSSCs are composed of a nanostructured semiconductor, a photosensitizer, an electrolyte and a counter electrode. For developing efficient DSSC devices, it is crucial to design and synthesize high-performance sensitizers as their properties significantly affect the DSSC performance. In recent years, boron dipyrromethene (BODIPY)-based dye-sensitized solar cells have gained a lot of attention because of their high photostability and excellent light absorption properties. Mao *et al.* reported a 2,6-disubstituted BODIPY with power conversion efficiency (η) of 5.31%.[119] The general working mechanism of the DSSC is as follows:

1. Under the influence of light, the molecules of a dye are excited from their ground state to an excited state (Step (1) and Fig. 6a).

2. Step (2) involves the transfer of an electron from the excited dye to the conduction band (CB) of TiO_2. Step (3) involves the reduction of the oxidized dye to its ground state *via* electron donation by I^- in a redox electrolyte (Step (3)). The TiO_2 CB substrate is where most of the electrons are located. The reduction of I_3^- results in the regeneration of I^- (Step (4) and Fig. 6a).

3. The transfer of electrons into the CB of TiO_2 enables recombination with the dye or with I_3^- (Steps (5) and (6)), which decreases the power conversion efficiency (η) of the DSSCs. A systematic representation of the DSSC assembly is shown in Fig. 6a, and the working mechanism is described as follows:

$$\mathrm{Dye/TiO_2} + h\nu \rightarrow \mathrm{Dye^*/TiO_2} \quad \text{(Step 1)}$$

$$\mathrm{Dye^*/TiO_2} \rightarrow \mathrm{Dye^+/TiO_2} + \mathrm{e^-(TiO_2)} \quad \text{(Step 2)}$$

$$\mathrm{2Dye^+/TiO_2} + \mathrm{3I^-} \rightarrow \mathrm{2Dye/TiO_2} + \mathrm{I_3^-} \quad \text{(Step 3)}$$

$$\mathrm{I_3^-} + \mathrm{2e^-(pt)} \rightarrow \mathrm{3I^-} \quad \text{(Step 4)}$$

$$\mathrm{Dye^+/TiO_2} + \mathrm{e^-(TiO_2)} \rightarrow \mathrm{Dye/TiO_2} \quad \text{(Step 5)}$$

$$\mathrm{I_3^-} + \mathrm{2e^-(TiO_2)} \rightarrow \mathrm{3I^-} \quad \text{(Step 6)}$$

It is possible to improve the efficiency of DSSCs by carefully determining the optimal significance of the many parameters that are involved in the fabrication process.

The various specific performance parameters of a dye-sensitized solar cell are the open-circuit voltage (V_{oc}), short-circuit current density (J_{sc}), fill factor (FF), maximum voltage (V_{max}) and maximum current density (J_{max}) (Fig. 6b).[74,121] An explanation of the performance parameters is as follows:

1. Open-circuit voltage: the open-circuit voltage is the difference in potential between the two terminals in the cell under light illumination when the circuit is open. The open-circuit voltage is measured when the current through the DSSC is zero (open circuit) and dependent on the cell temperature. At the open terminals of the DSSC, the voltage is mentioned as the open-circuit voltage.

2. Short-circuit current density: the short-circuit current density (J_{sc}) is the photocurrent per unit area (mA cm^{-2}) when an illuminated DSSC is short-circuited. This depends on several factors, such as the light absorption, light intensity, regeneration of the oxidized dye and the injection efficiency.

3. Fill factor: the ideality of the DSSC can be determined by the fill factor, which is defined as the ratio of the highest power output per unit area to the product of the open-circuit voltage and current density. This ratio is used to measure the DSSC.

4. Efficiency: in dye-sensitized solar cells, the overall solar energy to electrical conversion efficiency is defined as the maximum value of the cell output divided by the incident light power. It is estimated by measuring the photocurrent density at short circuit (J_{sc}), the open-circuit photovoltage (V_{oc}) at open-circuit terminals, the incident light intensity and the cell fill factor (FF).

The BODIPY unit represents a promising chromophore because of its vast variety of structural modifications for the design of suitable polymers or small molecules for use in organic solar cells. The absorption spectrum of BODIPY can be easily shifted towards the NIR region, which is useful for capturing sunlight; BODIPY dyes have therefore been used a lot in organic solar cells (OSCs) in previous years. The design and synthesis of a donor–acceptor (D–A)-type molecule is one of the most widely utilized strategies for tuning the optoelectronic properties. BODIPY dyes have been employed in organic

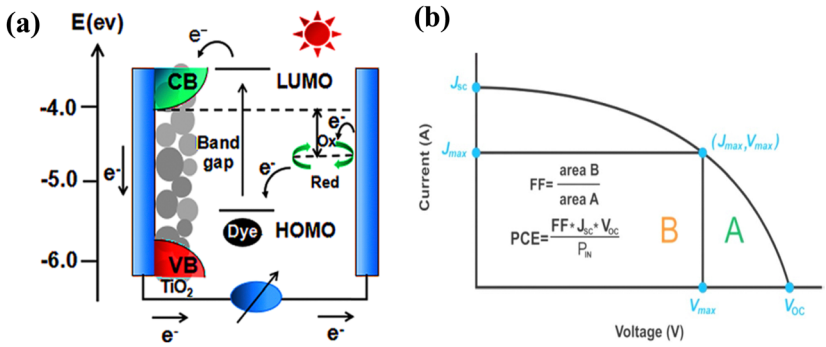

Fig. 6 (a) Schematic representation of the DSSC assembly. Reproduced from ref. 120 with permission from the American Chemical Society. (b) Performance parameters. Reproduced from ref. 121 with permission from Springer Nature.

photovoltaic devices as both donors and acceptors. Thayumanavana *et al.* reported an acceptor–donor–acceptor molecule containing a terminal acceptor BODIPY unit that exhibits a power conversion efficiency of 1.51%.[122] In 2018, Sharma *et al.* reported the BODIPY–thiophene co-polymer as a donor, with a power conversion efficiency of 9.3%.[123] Recently, Li *et al.* reported a BODIPY-based polymer with a power conversion efficiency of 9.86%.[124] In 2020, Vasilopoulou and co-workers reported pyrene–BODIPY-based donor–acceptor dyes for organic solar cells (OSCs), and power conversion efficiency values of 9.86 and 11.80% were obtained, respectively, for the fullerene and norfullerene devices. The photostability of the pyrene–BODIPY-based donor–acceptor dyes makes it possible for the OSC devices to operate reliably for a long time, which is a requirement of their future commercialization.[125] DSSCs provide several improvements over conventional silicon cells, including cheap production costs, flexibility, and a wide range of color options. Yeh *et al.* reported the 2,6-modified BODIPY dye for DSSCs with a power conversion efficiency of 6.4%.[126] In 2017, Kubo and co-workers reported the benzene-fused BODIPY dye conjugated with a phenothiazine unit as an anchoring moiety for DSSCs, with a power conversion efficiency of 7.69%.[127]

2.1.1. BODIPYs derived through vertical design. The vertical design model is the backbone for the majority of BODIPY dyes used in DSSCs. In this model, an anchoring group – commonly either benzoic acid or phenylcyanoacetic acid – is located at the *meso*-position of BODIPY. Kubota *et al.* synthesized the thiophene-fused BODIPYs **116** and **117** with two diethylaminophenyl groups as electron-donor units and investigated their photovoltaic performance (Fig. 7). BODIPYs **116** and **117** exhibit an absorption band at 783 nm and 813 nm and fluorescence maxima at 862 nm and 916 nm, respectively, in DCM solvent (Fig. 8a and b).

BODIPY **116** exhibits a higher fluorescence quantum yield (0.12) than BODIPY **117** (0.02). The thiophene-substituted BODIPY **117** shows a redshifted absorption band compared with the phenyl-substituted BODIPY **116** due to the strong electron-donating nature of the thiophene unit. BODIPY **116** exhibits a higher HOMO and LUMO gap of 1.51 eV, which is 1.44 eV in BODIPY **117** due to the weak donor ability of the phenyl unit compared with the thiophene unit. Thiophene-substituted BODIPY **117** exhibits easy intersystem crossing (ISC) compared with BODIPY **116** due to the heavy atom effect of sulfur at the *meso*-position of BODIPY. Phenyl-substituted BODIPY **116** and thiophene-substituted BODIPY **117** exhibit power conversion efficiency (η) values of 1.40% and 1.12%, respectively. The IPCE value for BODIPYs **116** and **117** was obtained as 18.1% at 790 nm and 12.3% at 810 nm, respectively. These IPCE results show that BODIPY **116** exhibits higher J_{sc} and η values than BODIPY **117** (Table 1).[128]

Shah *et al.* synthesized BODIPYs **118–121**, which are used as a photosensitizer in DSSCs (Fig. 7). BODIPYs **120** and **121** were synthesized by incorporating thienothiophene vinyl and bisthienyl vinyl chains in the molecular structures, which resulted in a redshift in the UV-visible absorption as well as increasing the IPCE. BODIPYs **120** and **121** exhibit two peaks in their absorption spectra: the first peak in 350–450 nm range is

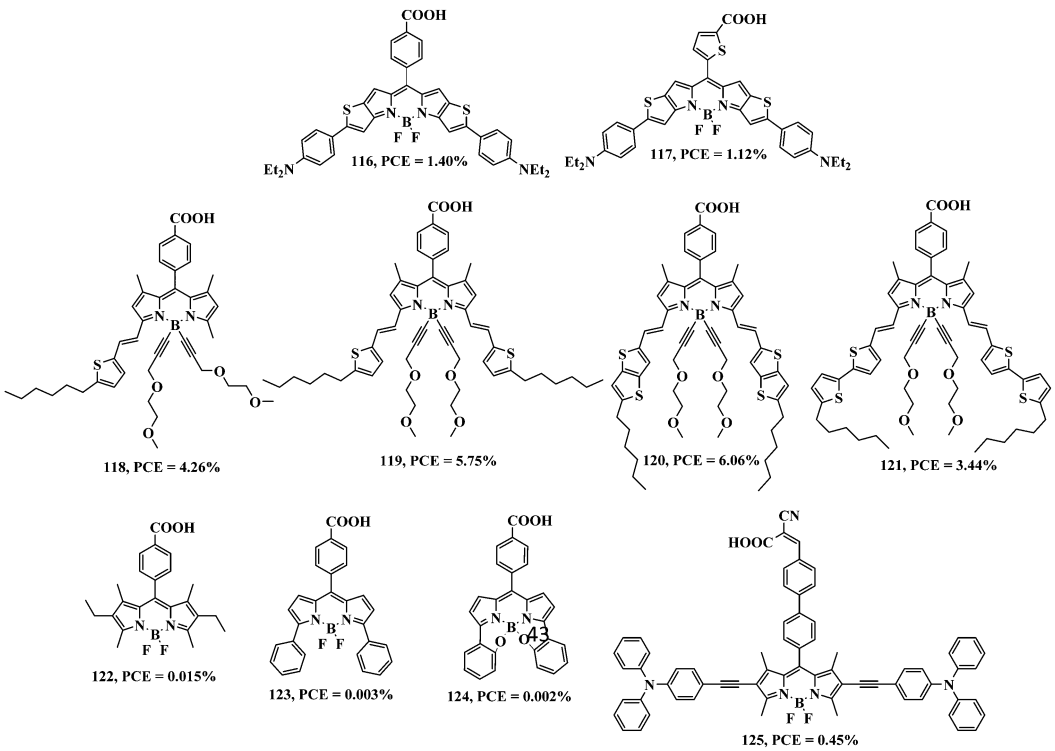

Fig. 7 Molecular structures of BODIPYs **116–125**.

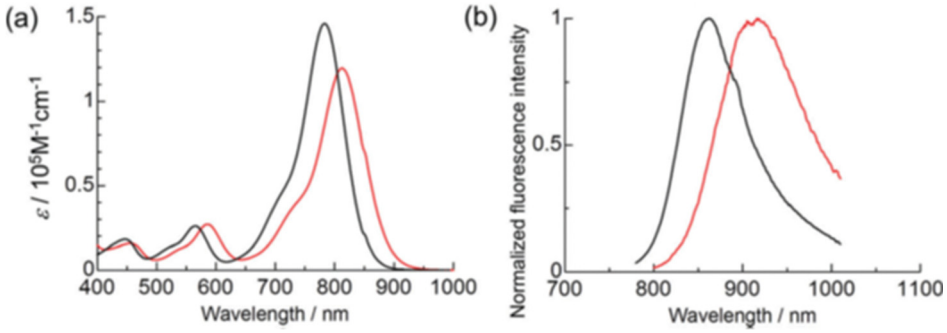

Fig. 8 (a) UV-vis-NIR absorption spectra and (b) normalized fluorescence spectra of BODIPYs **116** (black line) and **117** (red line) in dichloromethane (10^{-5} M). Reproduced from ref. 128 with permission from the Royal Society of Chemistry.

Table 1 Photovoltaic performance of BODIPY dyes

Dyes	J_{sc} (mA cm^{-2})	V_{oc} (V)	FF	η (%)
116	4.98	0.43	0.65	1.40
117	3.96	0.43	0.65	1.12
118	11.40	0.526	0.71	4.26
119	15.78	0.54	0.67	5.75
119 + **120**	17.80	0.55	0.68	6.76
120	16.10	0.53	0.70	6.06
121	12.00	0.45	0.62	3.44
122	0.56	0.07	0.38	0.015
123	0.58	0.02	0.28	0.003
124	0.42	0.02	0.29	0.002
125	1.26	0.55	0.64	0.45
N719 dye	7.09	0.64	0.67	3.09
N719 dye + 5% **125**	8.71	0.67	0.66	3.85
N719 dye + 10% **125**	5.02	0.64	0.66	2.10
126	0.76	0.45	0.54	0.18
127	1.04	0.52	0.60	0.32
128	3.18	0.58	0.69	1.28
129	15.03	1.15	—	11.79
130	27.25	1.07	—	19.91
131	28.61	1.03	—	20.19
132	38.01	1.02	—	26.54
133	39.79	1.00	—	27.27
134	9.69	0.53	0.71	3.70
135	15.43	0.54	0.71	6.02
135 + **134** (ratio 1 : 1)	16.07	0.56	0.68	6.20
136	16.4	0.80	0.68	8.93
137	26.2	0.63	0.68	11.25
138	26.2	0.68	0.68	12.13
139	27.2	0.73	0.68	13.5
140	1.66	0.45	0.59	0.44
141	1.31	0.44	0.60	0.35
142	0.73	0.32	0.47	0.11
143	0.63	0.25	0.52	0.09
144	0.38	0.08	0.37	0.008
145	0.51	0.22	0.43	0.05
146	1.66	0.49	0.52	0.42
147	3.40	0.67	0.51	1.70
148	4.00	0.69	0.52	2.10
149	4.70	0.72	0.52	2.50
150	2.50	0.68	0.50	1.20
151	3.40	0.70	0.51	1.70
152	5.10	0.75	0.50	2.70

attributed to the thienothiophene vinyl and bis-thienyl vinyl units, respectively; the second absorption peak at 695–710 nm is attributed to the $S_0 \rightarrow S_1$ transition of the BODIPY unit. The respective BODIPYs **120** and **121** exhibit fluorescence quantum yields of 0.15 and 0.05 and η values of 6.06% and 3.44% (Table 1).[129] Recently, Gibson and co-workers reported the synthesis of BODIPYs **122–124** and investigated their power conversion efficiencies for DSSCs (Fig. 7). These dyes exhibit different electronic properties, leading to different performance characteristics in DSSCs. Photophysical studies showed that the respective BODIPYs **122–124** exhibit an absorption band at 528 nm, 515 nm, 625 nm and an emission band at 536 nm, 541 nm, 654 nm. In BODIPY **124**, B–O coordination forces the phenyl unit towards the plane of dipyrromethane, and due to this the absorption and emission bands show a redshift compared with BODIPYs **122** and **123**. BODIPY **122** exhibits a high power conversion efficiency (η) compared with BODIPYs **123** and **124** (Table 1).[130] Wootthikanokkhan and co-workers reported the design and synthesis of triphenylamine-substituted BODIPY **125** and its use as a sensitizer in DSSCs (Fig. 7). The blue solution of BODIPY **125** exhibits an absorption band that covers the 300–700 nm range. The absorption peaks at 345 nm and 598 nm correspond to the TPA units, and are attributed to the π–π* transition and ICT transition, respectively. When BODIPY **125** was adsorbed onto a TiO_2 electrode, the longer-wavelength absorption band shifted to a higher wavelength region, from 598 nm in solution to 606 nm on TiO_2. The electrochemical analysis of BODIPY **125** shows an oxidation wave at 0.53 eV and a reduction wave at −1.10 eV. The co-sensitizer N719 dye/5% BODIPY **125** shows a higher power conversion efficiency (η) of around 5.14%, which is 66% higher than the device containing N719 dye (η = 3.09%) (Table 1).[131]

2.1.2. BODIPYs derived through horizontal design. In horizontal design, the anchoring group, such as phenylcyanoacetic acid or cyanoacetic acid, is linked with BODIPY through π-conjugation to synthesize a D–π–A-type system. Mao *et al.* reported imidazole-based BODIPYs **126–128** and investigated their photovoltaic performance for DSSCs. 4,5-Bis(4-methoxyphenyl)-1*H*-imidazole was used as the donor unit, BODIPY acted as a conjugate bridge and cyanoacetic acid was the acceptor unit (Fig. 9). BODIPYs **126–128** exhibit a UV-visible absorption band in the 250–675 nm range; the absorption peak in the 250–400 nm region was assigned to the π–π* transition, whereas for the longer wavelength region (420–650 nm) these intramolecular charge transfer transitions were assigned to the presence of the BODIPY unit. The respective power conversion

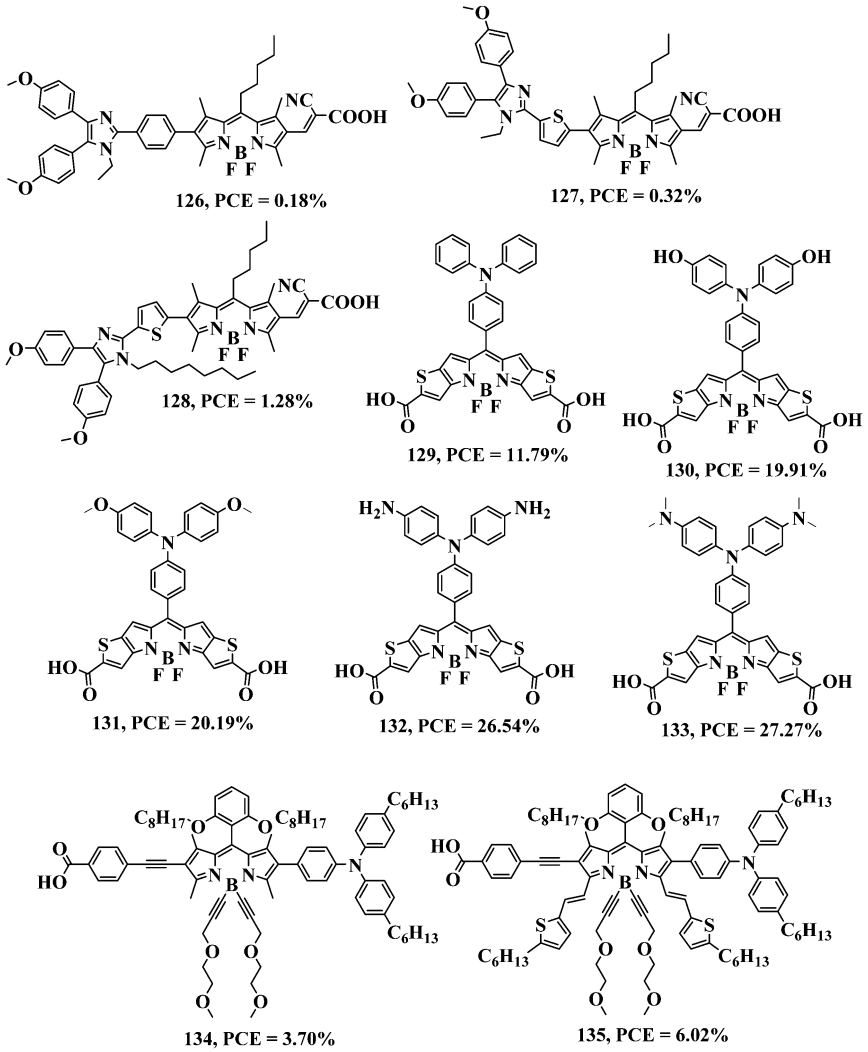

Fig. 9 Molecular structures of BODIPYs **126–135**.

efficiency (η) values of BODIPYs **126–128** are of 0.18%, 0.32%, and 1.28% (Table 1).

BODIPY **128** exhibits a high η compared with BODIPYs **126** and **127**, which is due to its better co-planar geometry and enhanced light-harvesting efficiency.[132] Liu *et al.* reported a set of *meso*-functionalized BODIPY-based D–π–A–A dyes **129–133** (Fig. 9). BODIPYs **129–133** exhibit absorption maxima at 572 nm, 570 nm, 567 nm, 546 nm and 548 nm, respectively, due to the transition from the HOMO to the LUMO (π–π* transition), and they exhibit power conversion efficiency (η) values of 11.79%, 19.91%, 20.19%, 26.54% and 27.27%, respectively. BODIPY **133** exhibits a high η of 27.27% compared with BODIPYs **129–132**, which show η values of between ∼11 and 26% (Table 1). The HOMOs of BODIPYs **129–133** are centered over the donor unit, whereas the LUMOs are mainly spread over the acceptor unit. The theoretically calculated HOMO–LUMO gap of BODIPYs **129–133** increases in the order **133** (1.70 eV) < **132** (1.86 eV) < **131** (2.01 eV) < **130** (2.07 eV) < **129** (2.21 eV). BODIPYs **129–133** have an acceptor BODIPY unit, so the large energy gap is caused mainly by the donor group and follows the order as $-N(CH_3)_2 > -NH_2 > -OCH_3 > -OH$.[120] In 2020, Islam and co-workers reported the α- and β-functionalized BODIPYs **134** and **135** for DSSCs (Fig. 9).[133] BODIPY **134** exhibits an absorption band at 553 nm and an emission band at 652 nm. The molar extinction coefficient value of BODIPY **134** is 54 000 M^{-1} cm^{-1}. BODIPY **134** exhibits a Stokes shift of 2600 cm^{-1}. BODIPY **135** exhibits three absorption bands, at 688 nm, 628 nm and 580 nm, and an emission maximum at 708 nm. The absorption band in the higher wavelength region was assigned to the $S_0 \rightarrow S_1$ transition. As determined from their UV-visible spectra, the optical bandgap values for BODIPYs **134** and **135** are 2.06 eV and 1.71 eV, respectively. Replacing the boron substituents with inert alkynyl-oligoethylene glycol chains has been proved to be a viable technique for enhancing both the solubility and stability as well as to prevent aggregation of the dye. DSSCs sensitized with BODIPY **135** have a high photovoltaic response in the UV-visible-to-NIR region with an IPCE of 60% in the 350–720 nm range and η = 6.02%. The η and IPCE values of BODIPY **134** at 530 nm are 3.7% and 71%, respectively. From the simultaneous use of both BODIPYs **134**

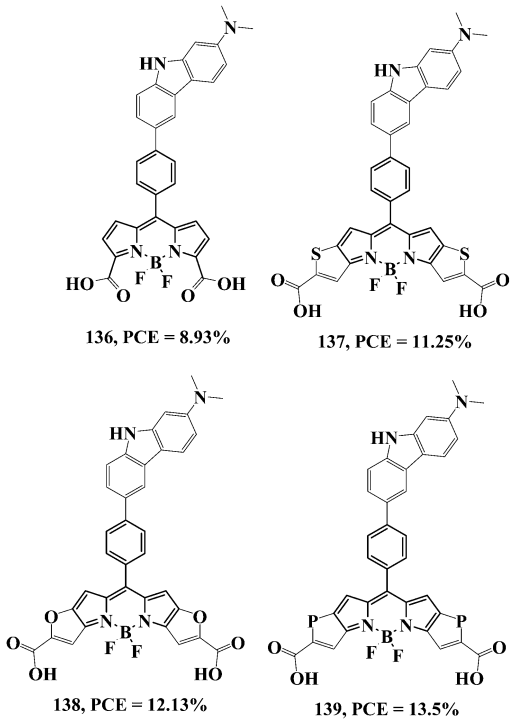

Fig. 10 Molecular structures of BODIPYs **136–139**.

and **135** as a co-sensitizer in DSSCs, the power conversion efficiency (η) was improved to 6.2% due to their complementary absorption properties (Table 1).[133]

Metal-free organic dyes with push–pull structures are beneficial due to their easy functionalization, which enhances the light-harvesting ability, achieving a high molecular extension coefficient and resulting in high-performance DSSCs. Rahman *et al.* reported BODIPYs **136–139** *via* the rational design of BODIPY–carbazole (D–π–A–A) dyes for DSSCs (Fig. 10).[134]

The BODIPY–carbazole structure was altered by introducing an electron-donating $-N(CH_3)_2$ group at the electron-donating carbazole moiety and two electron-withdrawing –COOH groups at the BODIPY core. BODIPY **136** was modified further through the introduction of heterocyclic rings to synthesize BODIPYs **137–139**, which show a redshift in the absorption spectra and increase the light-harvesting efficiency. The respective BODIPYs **136–139** exhibit absorption maxima at 467 nm, 518 nm, 519 nm and 527 nm. BODIPY **139** exhibits a maximum power conversion efficiency of 13.5% compared with BODIPYs **136–138** (Table 1). The structurally configured BODIPY **139** can be used as a potential photosensitizer for high-performance DSSCs.

2.1.3. BODIPYs derived using other design strategies. Numerous other methods for improving the photovoltaic performance of BODIPY dyes in DSSCs were summarized. Yildiz *et al.* reported a series of BODIPY derivatives (**140–143**) that contain methoxyphenyl or triphenylamine (TPA), and investigated their photovoltaic properties for DSSC applications (Fig. 11). The triphenylamine or methoxyphenyl unit at the C8-position and the catechol moieties at the C3 and C5-positions were incorporated into the BODIPY, which increases the electron transfer mechanism and the DSSC performance.[135] The absorption spectra of BODIPYs **140–143** exhibit absorption bands in the higher-wavelength region, at 574 nm, 576 nm, 650 nm and 652 nm, respectively. BODIPYs **140–143** show a strong absorption band at the higher wavelength due to the $S_0 \rightarrow S_1$ transition, whereas at lower wavelengths the transition corresponds to $S_0 \rightarrow S_2$. An emission band was observed at 610 nm for BODIPYs **140** and **141** and at 675 nm for BODIPYs **142** and **143**. The fluorescence intensity decreases in the TPA-containing BODIPYs **142** and **143** due to the increasing

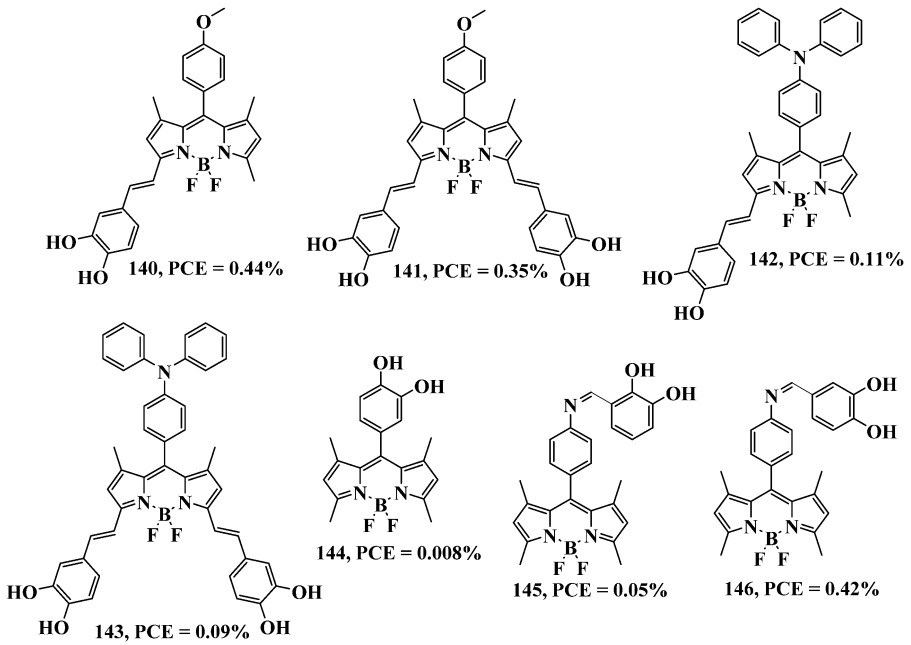

Fig. 11 Molecular structures of BODIPYs **140–146**.

intramolecular charge transfer. The methoxyphenyl group has a more efficient electron injection process compared with the TPA unit. The power conversion efficiency (η) values of the respective BODIPYs **140–143** are 0.44%, 0.35%, 0.11%, and 0.09% (Table 1).

Hayvali *et al.* reported BODIPYs **144–146** and investigated the CT effect dynamics on the photovoltaic behavior in DSSCs (Fig. 11). Attaching the catechol group at different positions of the phenyl ring in addition to the conjugation length of the catechol-containing unit significantly affect the DSSC performance.[136] The respective BODIPYs **144–146** show absorption maxima in the 450–550 nm region, which corresponds to the $S_0 \rightarrow S_1$ transition, whereas absorption maxima in the 250–420 nm region are assigned to the $S_0 \rightarrow S_2$ transition. BODIPYs **144** and **146** exhibit a higher fluorescence intensity compared with BODIPY **145**, and the broad emission around 550 nm is due to the fluorescence signal from the charge transfer (CT) state. The photovoltaic performance of BODIPYs **144–146** showed power conversion efficiency (η) values of 0.008%, 0.05% and 0.42%, respectively (Table 1). Saravanan *et al.* synthesized triazole-based BODIPY dendrimers **147–149** as photosensitizers for DSSC applications (Fig. 12).[137] The respective BODIPYs **147–149** showed absorption maxima at 386 and 499 nm, 385 and 500 nm, 384 nm and 501 nm due to presence of the triazole and BODIPY units (Fig. 13a). The fluorescence spectra of BODIPYs **147–149** exhibit an emission band at 507, 508 and 509 nm, respectively, when excited at 490 nm (Fig. 13b). The fluorescence quantum yields of BODIPYs **147–149** are 0.18, 0.34 and 0.46, respectively. The fluorescence intensity of BODIPYs **147–149** increases as the number of triazolyl and BODIPY units increases. Generally, BODIPY exhibits one oxidation and one reduction wave at low potential. The redox properties of BODIPYs **147–149** show a reversible oxidation potential at 662 mV, 638 mV and 600 mV and a reversible reduction potential at 594 mV, 575 mV and 522 mV, respectively. The oxyethylene chains ensure chemical stability while the tris-BODIPY-based supramolecular structure promotes extension of the π-conjugated system and hence decreases the HOMO–LUMO energy gap. The BODIPY- and triazole-containing dendrimers show excellent power conversion efficiency (η) values, in which the triazole is responsible for absorption of the dye at the TiO_2 surface, and the BODIPY unit improves the solar energy-harvesting efficiency in DSSC applications. BODIPYs **147–149** are strongly absorbed on the TiO_2 surface and show power conversion efficiency (η) values of 1.7%, 2.1% and 2.5%, respectively, in DSSC applications (Table 1).[137]

Rajakumar and co-workers reported BODIPY dendrimers **150–152**, which contain 3,6-di-*tert*-butyl carbazole and triazole as the bridging unit, and explored their photophysical and redox properties (Fig. 14). BODIPY dendrimers **150–152** exhibit two absorption bands, where the first absorption band at 297 nm is attributed to the π–π* transition, and the second absorption band at 503–505 nm is attributed to the π–π* transition ($S_0 \rightarrow S_1$) of BODIPY. BODIPYs **150–152** exhibit three emission bands, at 355 nm, 370 nm and 370 nm, when the excitation wavelength is 297 nm. The fluorescence quantum yields of BODIPYs **150–152** are 0.12, 0.37 and 0.44, respectively. Electrochemical studies of BODIPY dendrimers **150–152** showed multiple redox waves, which are due to the presence of the redox-active carbazole, triazole, and BODIPY units. BODIPY dendrimer **152** exhibits a better power conversion efficiency (η) of 2.7% compared with BODIPY dendrimers **150** and **151** (Table 1).[138]

2.2. Photodynamic therapy (PDT)

Cancer is a perpetual threat to human health because of its high morbidity and mortality worldwide. Cancer currently affects 0.5% of the world population each year, with 25% of cancer patients dying. Cancer is uncontrolled cell proliferation that can spread throughout the body and cause death.[139] Fluorescent dyes are utilized widely in chemical, environmental and biological sciences because of their superior sensitivity, photochemical stability and accessibility. Photodynamic therapy (PDT) offers an effective means of killing cancer cells with little risk of harming healthy cells. The PDT mechanism involves a photosensitizer that can damage/kill the target cells upon light irradiation. Photodynamic therapy uses photosensitizers that absorb energy and transfer it to the surrounding oxygen molecules. This produces singlet oxygen ($^1O_2$) species, which can destroy cancer cells through reaction with the surrounding biological molecules (Fig. 15). Molecules/dyes that contain a heavy metal ion or bulky Br or I lead to the ISC (intersystem crossing) process, which helps to generate the highly reactive and cytotoxic singlet oxygen species for destroying the cancer cells. The photophysical properties of the BODIPY dye can be tuned *via* specific structural modification/functionalization around the core. The rational molecular design of BODIPY dyes is a strategy used to increase the $^1O_2$ quantum yield for photodynamic therapy. This approach is relevant for the design and synthesis of three classes of BODIPY dyes, namely halogenated BODIPY, BODIPY dyads and BODIPY dimers.[75,140] The simple method of post-functionalization *via* halogenation is used for the synthesis of halogenated BODIPYs. The approach towards BODIPY dyads involves the synthesis of BODIPY dyes by incorporating suitable substituents at the *meso*-position. In the case of BODIPY dimers, either post-functionalization of the BODIPY monomer or construction of the linked framework is considered for the synthetic approach. Akkaya and co-workers reported the preparation of bromo-substituted styryl BODIPYs *via* the Knoevenagel reaction to achieve high singlet oxygen ($^1O_2$) yields for PDT.[141] Flamigni and co-workers reported the first halogen-free photosensitizers based on the orthogonal-BODIPY dimer and achieved significant $^1O_2$ generation.[142]

To expand the use of PDT in medical applications, two-photon photodynamic therapy (TP-PDT) is proposed in which two NIR photons are utilized for photosensitizer activation rather than a single photon. TP-PDT has been demonstrated to offer a better spatial selectivity and penetration depth, enabling the treatment of tiny infected areas without affecting the surrounding normal tissue, as well as the treatment of solid

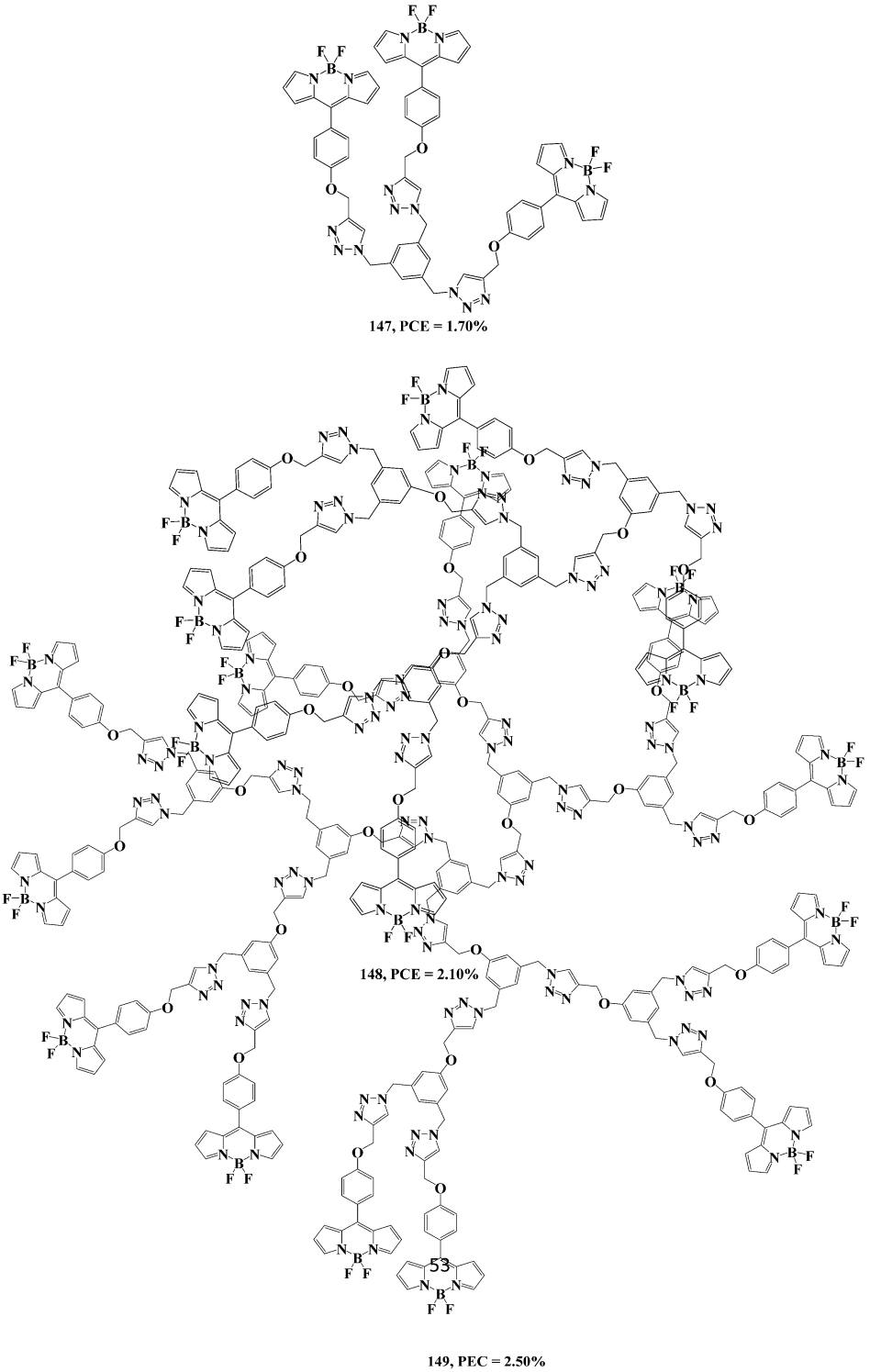

Fig. 12 Molecular structures of BODIPY dendrimers **147–149**.

and deeper tumors. High spatial selectivity is required for diseases related to the eye and brain.[143] The two-photon efficiency of organic photosensitizers can be improved *via* increasing the π-conjugation.[144] The groups of Ziessel and Burgess explored the design, synthesis and structural modifications of BODIPY chromophores for biomedical applications.[145,146]

Photodynamic therapy (PDT) requires three main components: a photosensitizer (PS), light and oxygen (O_2). Under irradiation, the activated PS can transfer its excited-state energy to O_2 and water to generate toxic reactive oxygen species (ROS) to induce cancer cell death.[147] In general, when molecules absorb energy they are excited to a higher energy level and

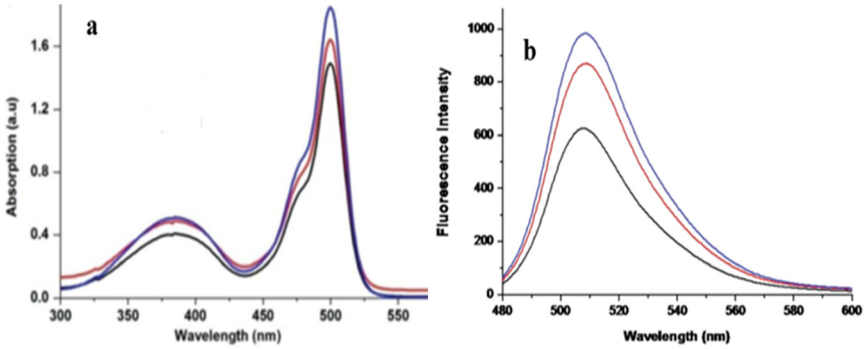

Fig. 13 (a) UV-visible absorption spectra and (b) fluorescence spectra of BODIPY dendrimers **147** (black), **148** (red), and **149** (blue) in DCM (1×10^{-5} M) at room temperature. Reproduced from ref. 137 with permission from the Royal Society of Chemistry.

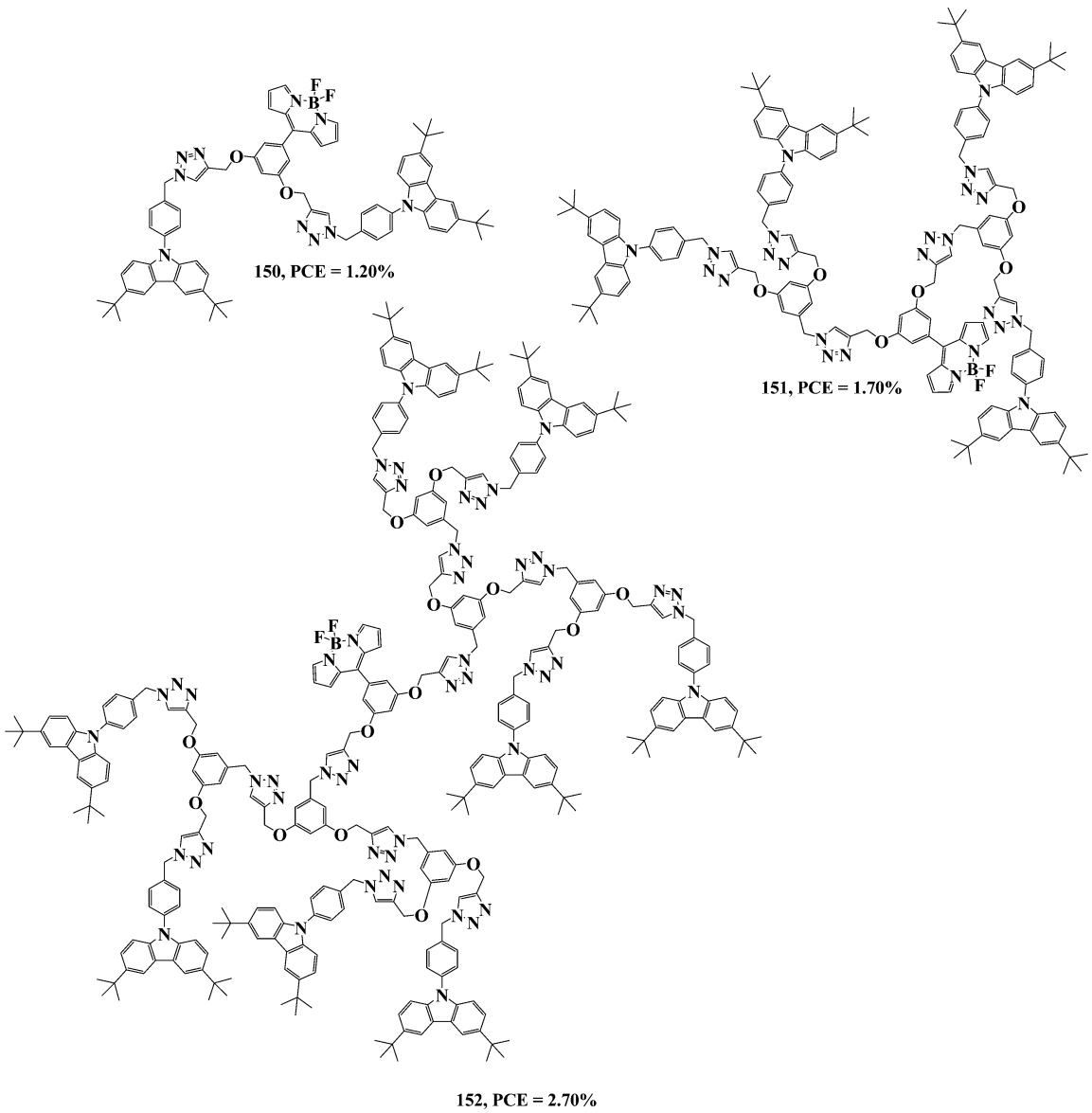

Fig. 14 Molecular structures of BODIPYs **150–152**.

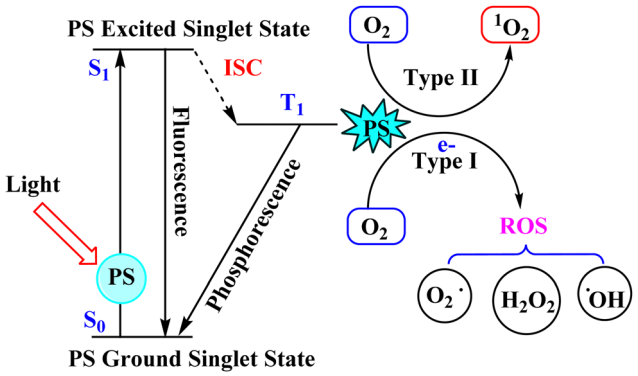

Fig. 15 Schematic representation of photodynamic therapy using the Jablonski diagram.

return to their lowest energy level *via* three distinct molecular processes. which are as follows:

1. Non-radiative processes: when a molecule is excited, it relaxes *via* transferring to other energy levels, either vibrational or electronic. Internal conversion, inter-system crossing, and vibrational relaxation are three examples of such processes. Energy is released in the form of heat during these processes (Fig. 15).

2. Radiative processes: phosphorescence and fluorescence are radiative processes in which energy is released in the form of electromagnetic radiation, *e.g.*, light (Fig. 15).

3. Other routes of deactivation: excited molecules go through a process called photosensitization when they are exposed to light. This may result in any kind of chemical or physical reaction to give different results.

The photosensitizer uses oxygen molecules to produce reactive oxygen species (ROS) in their excited state, a process which is known as ''photodynamic action''. There are two primary routes for this: type-I and type-II.

Type-I mechanism: in this process, an excited state (triplet) PS transfers an electron or hydrogen to a substrate, resulting in the production of a free radical, which then reacts with oxygen to produce active species such as $^{\bullet}OH$, $O_2^{\bullet}$ or H_2O_2, setting off a chain reaction that produces more radicals (Fig. 15).

Type-II mechanism: in this case, the PS goes from its ground state to its triplet excited state, transferring its energy to O_2 to produce singlet oxygen ($^1O_2$) by absorbing electrons from aromatic rings such as phenols, amines and thioethers (Fig. 15).

2.2.1. Classification of BODIPYs

2.2.1.1. Halogenated BODIPYs. BODIPY derivatives are able to undergo a wide variety of different modifications, and they possess many useful properties such as low toxicity, cellular uptake, high extinction coefficients and low quantum yields for PDT. In PDT, photo-damage occurs in triplet excited states, so for PDT applications it is preferential that BODIPY dyes are modified to improve intersystem crossing (ISC). Halogenation is the most popular method of such modification and involves heavy halogen atoms, which is called the ''heavy atom effect''.[148] In 2020, Liu *et al.* synthesized BODIPY **153** and investigated its performance in photodynamic tumor therapy (Fig. 16). The incorporation of halogen atoms Br or I at the 2- and 6-pyrrolic positions of the BODIPY core significantly increased the efficiency of singlet oxygen generation, which is useful for photodynamic therapy. The $^1O_2$ generation property of the BODIPY **153** can be quenched *via* the aggregation behavior and PET (photoinduced electron transfer) effect of the dimethylaminophenyl unit, which results in low toxicity. BODIPY **153** shows good photostability in both neutral and acidic conditions. In addition, BODIPY **153** was activated under acidic conditions, and the protonated form of BODIPY **153** was successfully disaggregated *via* enhanced solubility and space charge repulsion in order to activate photodynamic therapy. Cytotoxicity studies revealed that BODIPY **153** can kill cancer cells effectively under light irradiation. Thus, photosensitizer **153** inhibits tumor growth strongly under acidic conditions with light irradiation.[149]

In 2019, Xie and co-workers reported the preparation of 2,6-diiodo-BODIPY **154** *via* non-covalent interactions between carbon dots and BODIPY (Fig. 16). BODIPY **154** exhibits a high PDT effect through the FRET (fluorescence resonance energy transfer) phenomenon with a fluorescence quantum yield of 23.9% (Table 2). The absorption intensity of the indocyanine

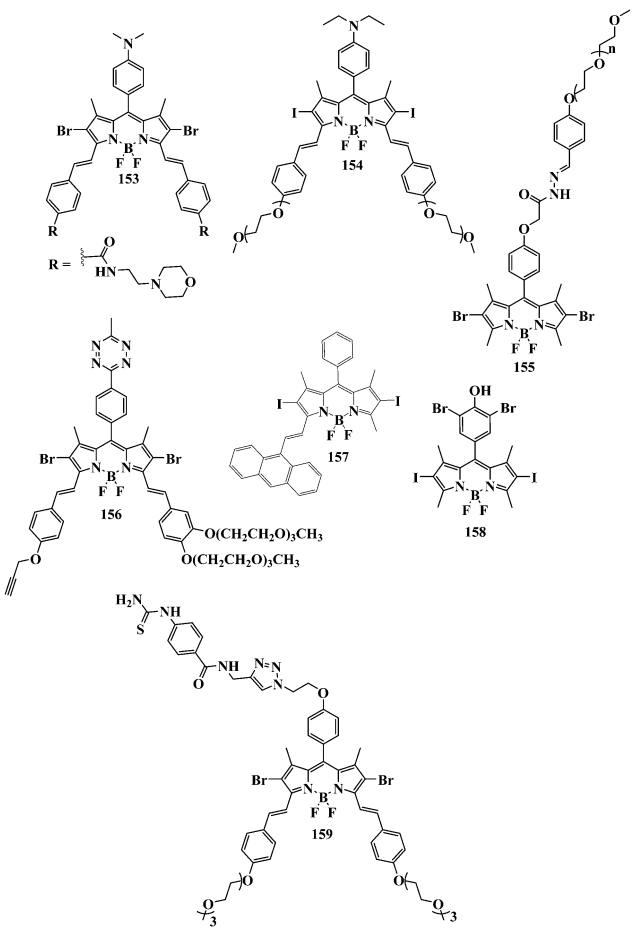

Fig. 16 Molecular structures of BODIPYs **153–159**.

Table 2 Fluorescence quantum yields, singlet oxygen quantum yields, photothermal conversion efficiency, phototoxicity, laser wavelength and references of the BODIPY dyes

Dyes	Fluorescence quantum yield (%)	Singlet oxygen quantum yield (%)	Photothermal conversion efficiency (η) (%)	Phototoxicity	Laser wavelength (nm)	Ref.
154	23.9	—	—	—	625	150
155	—	68	—	—	—	151
156	2	—	—	—	—	152
157	—	70	38.9	6.2 μg mL^{-1}	660	153
158	2	—	—	8.5 μM	532	154
159	—	52	—	—	660	155
160	12.3	73	—	—	808	156
161	5.0	95	—	0.4 μM	—	157
162	—	—	42.01	—	685	158
163	56	52	—	—	670	159
164	—	—	—	6 μM	640	160
165	—	—	—	28.5 μM	—	161
166	10	68	—	0.45 μM	—	162
167	—	—	—	197 μM	—	163
168	—	—	—	178 μM	—	163
169	24	19	—	40–52 μM	660	164
170	3.2	48	—	44 μM	660	164
171	72	—	34.1	—	660	165
172	66	—	35.2	—	660	165
173	68	—	54.5	—	660	165
174	70	—	58.3	—	660	165
175	78	—	76.7	12–15 μM	660	165
176	5.69	20.12	—	>12 μM	—	166
177	—	20	—	<5.0 μM	—	167
178	—	6	—	—	—	167
179	—	—	37	—	685	158
180	—	77	—	0.049–0.005 μM	—	168
181	30	—	—	—	—	169
182	4.0	—	—	—	—	169
183	2.0	—	—	—	—	169
184	08	—	50.9	26.5 μg mL^{-1}	635	170
185	31	55	—	1 μM	559	171

green dye decreases in the presence of BODIPY **154**, which shows a high PDT effect.[150] Recently, Chang *et al.* reported the β-dibromo-substituted BODIPY **155** (Fig. 16). The hydrazone bond of BODIPY **155** can be cleaved under acidic conditions (such as in the cancer cell environment), which is a desirable property of advanced therapeutic agents. BODIPY **155** was used as a photosensitizer to effectively generate $^1O_2$ in response to light irradiation, which results in high toxicity to the target cells (Table 2).[151] In 2019, Lo and co-workers reported distyryl-based BODIPY **156**, which contains 1,2,4,5-tetrazine and alkyne units (Fig. 16). BODIPY **156** exhibits absorption bands at 320 nm, 385 nm and 670 nm, which belong to π–π* transitions. A weak fluorescence band was observed at 710 nm with a low fluorescence quantum yield of 0.02 due to presence of two Br atoms (the heavy atom effect) (Table 2). The effectiveness of BODIPY **156** was demonstrated successfully in tumor-bearing mice. The emission intensity of BODIPY **156** was enhanced at the tumor site over time (Fig. 17). The fluorescence intensity was not enhanced without pre-treatment with TCO-GE11 (a non-fluorescent peptide) (Fig. 17). These results shows that BODIPY **156** can be useful as a photosensitiser for photodynamic therapy application.[152]

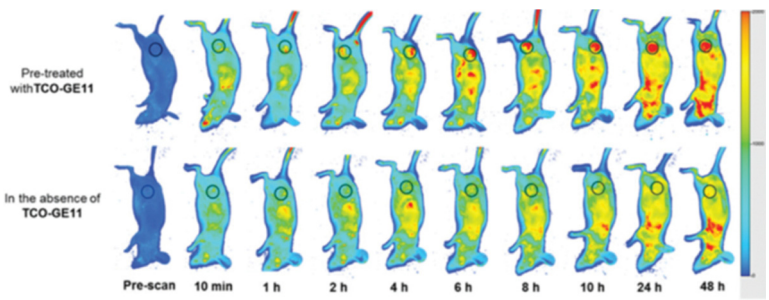

Fig. 17 Fluorescence image of A431 tumor-containing nude mice before and after treatment using BODIPY **156** with or without the injection of TCO-GE11. Reproduced from ref. 152 with permission from the Royal Society of Chemistry.

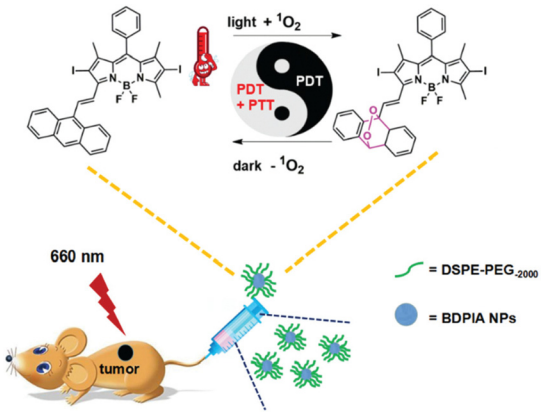

Fig. 18 Representation of BODIPY **157** nanoparticles for PDT and the mechanism of reversible $^1O_2$ capture and delivery. Reproduced from ref. 153 with permission from the Royal Society of Chemistry.

In 2019, Zhang and co-workers reported anthracene-substituted BODIPY **157** and investigated its singlet oxygen ($^1O_2$) storage ability for PDT (Fig. 16). During the light cycle, the anthracene module can be used to attract $^1O_2$ and convert it into endoperoxide. However, the endoperoxide undergoes thermal cycloreversion during the dark cycle to generate $^1O_2$, hence regenerating the anthracene module (Fig. 18). Nanoparticles of BODIPY **157** in water exhibit a high photothermal conversion efficiency (η = 38.9%) for successful PDT (Table 2). An *in vivo* fluorescence imaging study suggested that nanoparticles of BODIPY **157** can inhibit tumor growth under laser irradiation without any harmful effects on healthy cells. Such BODIPY nanoparticles that show high phototoxicity and good biocompatibility can be used as a photosensitizer in photodynamic therapy.[153]

Radunz *et al.* reported the pH-activatable singlet-oxygen-generating BODIPY **158** as a photosensitizer for PDT (Fig. 16). The pH-sensitivity of BODIPY **158** was obtained by including Br and OH groups, which are capable of photoinduced electron transfer, at the *meso*-position of the BODIPY unit. To facilitate the triplet state formation, iodine was introduced into the BODIPY core at both the 2- and 6-positions, which is necessary for generating singlet oxygen. pH-dependent studies demonstrated the cytotoxicity performance of BODIPY **158** in HeLa cells. BODIPY **158** exhibits good photostability and neither decomposes nor photobleaches within the time frame studied. Heavy halogen groups, such as iodine and bromine, were incorporated in this BODIPY to increase the intersystem crossing rate from $S_0 \rightarrow S_1$ *via* spin–orbital coupling, which increases the quantum yield for singlet oxygen generation. BODIPY **158** shows electronic absorption and emission bands at 534 nm and 550 nm, respectively. Light-activated photosensitizers can transfer energy to the surrounding oxygen molecules, resulting in the generation of $^1O_2$ and ROS.[154] Recently, Jung *et al.* reported phenylthiourea-substituted BODIPY **159** as an effective photosensitizer for PDT application (Fig. 16). Heavy bromo groups were introduced at the β-positions of the BODIPY unit to increase the generation of singlet oxygen (Table 2). Melanin is a primary absorber in the spectral band between 500 and 600 nm and is responsible for a reduction in the photoreaction efficiency of a photosensitizer. BODIPY **159** exhibits an absorption band at 667 nm, an emission band at 712 nm, and shows very good photostability. In different solvents it shows an electronic absorption band between 665 and 667 nm. The formation of intercellular reactive oxygen species and cell viability studies showed the significant photocytotoxic effects of BODIPY **159** on tyrosinase-positive melanoma cells (B16F10).[155] Liu *et al.* reported the photosensitizer BODIPY **160**, which shows good biocompatibility, low toxicity and a strong singlet oxygen quantum yield to prevent tumor growth in living cells (Fig. 19). Photosensitizer **160** contains the 4-(dimethylamino)benzaldehyde group, to increase the conjugation length and shift the emission band towards the NIR region. The iodine atoms at the 2- and 6-positions increase the efficiency of singlet-to-triplet intersystem crossing. BODIPY **160** shows an absorption maximum at 737 nm and a fluorescence quantum yield of 12.3% (Table 2). Nanoparticles of BODIPY **160** exhibit strong luminescence in the NIR-II window (1000–1700 nm) and a high $^1O_2$ quantum yield (0.73), enabling the formation of $^1O_2$ upon irradiation to kill cancerous cells and avoid harming healthy cells.[156]

In 2019, Wang *et al.* synthesized BODIPY **161**, which exhibits a singlet oxygen quantum yield of 0.95 and a fluorescence quantum yield (Φ_F) of 0.05 in EtOH solvent (Table 2), for photodynamic therapy applications (Fig. 19). BODIPY **161** exhibits an electronic absorption band at 545 nm and an emission band at 572 nm. The effect of heavy-atom iodine and sulfur promote the ISC process, resulting in the high generation of singlet oxygen ($^1O_2$). Photosensitizer BODIPY **161** shows pH-dependent singlet oxygen ($^1O_2$) generation, low dark toxicity and high phototoxicity towards the tumor cell line Bel-7402. In addition, photosensitizer BODIPY **161** exhibits high phototoxicity with only a minimum amount of light illumination.[157] In 2019, Xie and co-workers reported the amphiphilic photosensitizer BODIPY **162**, which contains the

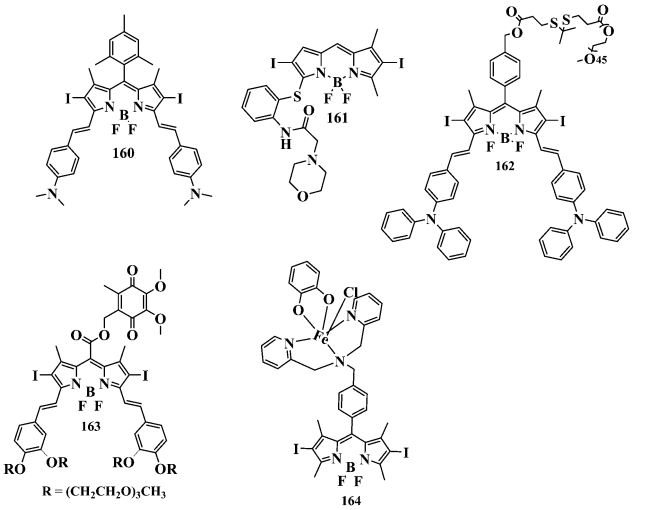

Fig. 19 Molecular structures of BODIPYs **160–164**.

BODIPY unit and a poly(ethylene glycol) unit connected by a thioketal linker for reactive oxygen species (ROS) generation (Fig. 19). Nanoparticles of BODIPY **162** provide heat and ROS upon irradiation for PDT (Table 2). The incorporation of iodine atoms at the 2- and 6-positions of the BODIPY core promotes ISC and generates $^1O_2$ under light irradiation. BODIPY **162** nanoparticles (5 μM) kill cells through photothermal and photodynamic effects. To study the thermal properties of BODIPY **162** the temperature rise and fall of the nanoparticles (NPs) was examined. The temperature of the BODIPY **162** NPs increased to 50 °C (after four cycles). The signal intensity of BODIPY **162** increased gradually upon increasing the NP concentration (Fig. 20a), where a histogram of the signal quantization is displayed in Fig. 20b. The *in vivo* imaging properties of BODIPY **162** were studied in live mice, and after 2 h the signal of BODIPY **162** in the tumor cells was clearly visible, as shown in Fig. 20c.

After the tail-vein injection of BODIPY **162** nanoparticles, *in vivo* near-infrared fluorescence imaging of the tumor tissue at different times was carried out, as highlighted by the white circles shown in Fig. 20d. After 6 h, fluorescence appeared in the tumor cells, which suggests that the nanoparticles are have reached the cancer cells.[158] Hwang *et al.* reported BODIPY **163** for PDT applications (Fig. 19). BODIPY **163** nanoparticles (NPs) exhibited high chemo- and photo-stability, as well as strong "turn-on" fluorescence and photosensitizing activities. The increase in emission intensity and $^1O_2$ generation reveals that BODIPY **163** is a potential photosensitizer for PDT applications. BODIPY **163** shows a strong absorption band at 711 nm ($\varepsilon = 9.5 \times 10^4$ M^{-1} cm^{-1}) and a low emission band at 756 nm in DMSO solvent. The reduction of ubiquinone to the hydrophilic carboxylate resulted in increased fluorescence and the generation of therapeutic singlet oxygen ($^1O_2$) (Table 2).[159] Recently, Chakravarty and co-workers reported the iron(III) catecholate of BODIPY **164** containing the dipicolylamine ligand, which shows a ligand-to-metal charge transfer (L→M CT) band at ~800 nm (Fig. 19). This mitochondria-localizing complex shows apoptotic cell death involving the generation of ROS from 2,7-dichlorofluorescein diacetate (DCF-DA). *In vivo* results show that iron-based infrared-active BODIPY **164** is useful for PDT.[160]

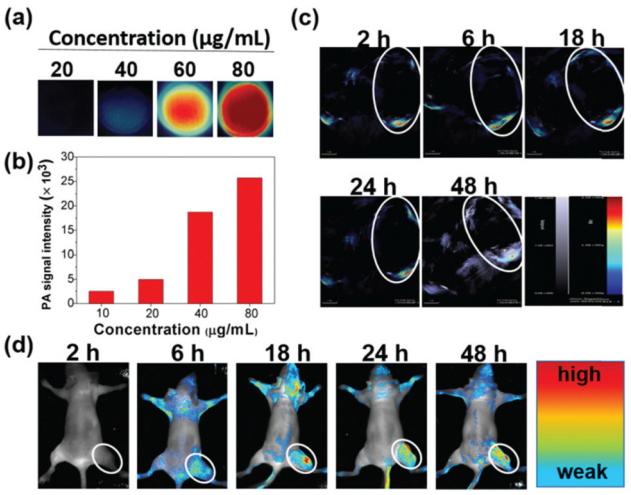

Fig. 20 Imaging properties of BODIPY **162** nanoparticles. Reproduced from ref. 158 with permission from the Royal Society of Chemistry.

2.2.1.2. Halogen-free BODIPYs. There is nothing particularly unique about halogen atoms in the development of BODIPY derivatives for triplet sensitization; any substituent with molecular orbitals that possess the appropriate multiplicity and energy levels can act as a sensitizer. Wang *et al.* reported BODIPY **165**, which exhibits two hydrophobic chains, and explored its performance in cell imaging and PDT (Fig. 21). Fluorescent BODIPY **165** shows low dark toxicity as well as photocytotoxicity at low concentrations for MCF-7 and HeLa cells. A high concentration of BODIPY **165** generates a large amount of ROS (reactive oxygen species) under white light and shows high phototoxicity to cancer cells. BODIPY **165** exhibits good photostability and a strong affinity for cell membranes, which makes it a good candidate for imaging applications. The photoinduced electron transfer phenomenon does not occur in BODIPY **165**, which is useful for bioimaging and photodynamic therapy applications.[161] Wang *et al.* reported the carbazole-based orthogonal donor–acceptor BODIPY **166** for PDT in living cells (Fig. 21). The tri-ethylene glycol monomethyl ether unit was attached at the 9-position of the electron-donor carbazole unit to increase the water solubility of the photosensitizer. BODIPY **166** exhibits an absorption band at 497 nm and a shoulder peak at 470 nm, and a fluorescence band was obtained at 511 nm with a low quantum yield of 0.1 (Table 2). BODIPY **166** exhibits a strong $^1O_2$ sensitizing ability ($\Phi_\Delta = 0.68$ in MeOH), excellent photostability and high phototoxicity (IC_{50} 0.45 μM) towards Bel-7402 tumor cells. The growth of tumor cells was effectively suppressed by BODIPY **166** under light illumination, which indicates that it is a potential photosensitizer for PDT applications.[162] Recently, Turkoglu *et al.* reported the distyryl-based BODIPYs **167** and **168**, which exhibit imidazole and tertiary amine units, respectively, for photodynamic therapy applications (Fig. 21). The heavy atom-free photosensitizer BODIPYs **167** and **168** show excellent photodynamic activity against MCF7 cells. The photophysical properties of BODIPYs **167** and **168** exhibit an absorption band at 627 nm and 625 nm, whereas the emission band is at 640 nm and 635 nm, respectively. BODIPYs **167** and **168** show photodynamic action in which the red emission intensity decreases upon $^1O_2$ generation. These photodynamic activity studies reveal that, at a micromolar concentration, the photosensitizers produce $^1O_2$ effectively and stimulate cell death in MCF7 cells.[163]

Chakravarty and co-workers reported the methyl malonyl chloride-derived monostyryl BODIPY **169** and the cisplatin-based complex BODIPY **170** for application in photodynamic therapy (Fig. 21). The cisplatin-based complex BODIPY **170** shows an absorption band at 616 nm and an emission band at 720 nm. Its high stability with low bleaching properties makes it a good candidate for bioimaging and PDT

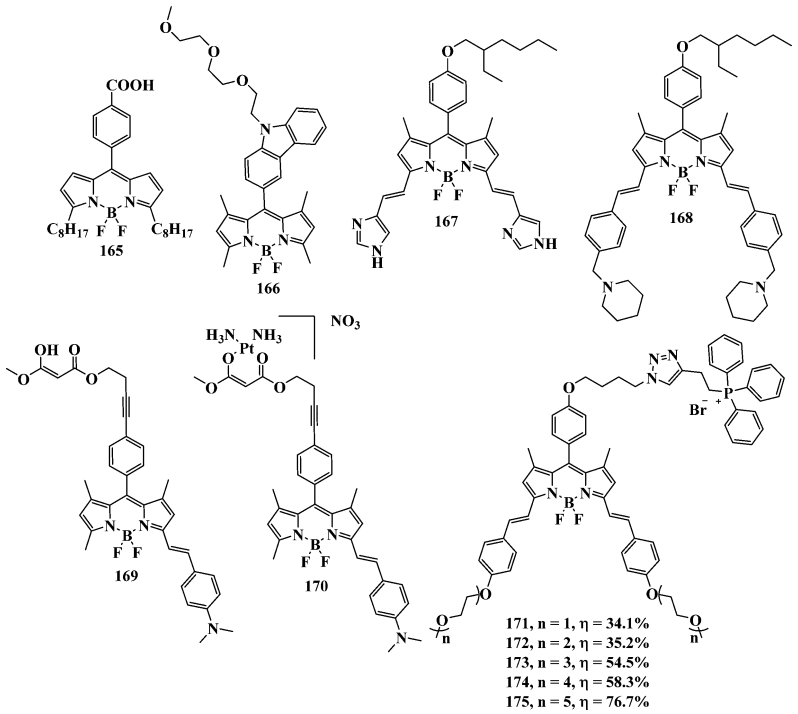

Fig. 21 Molecular structures of BODIPYs **165–175**.

applications. The fluorescence quantum yield values for BODIPYs **169** and **170** were 0.24 and 0.032, respectively (Table 2).[164] Wang *et al.* reported a set of mitochondria-targeted BODIPY nanoparticles **171–175** that contain cationic triphenylphosphine (TPP) and different numbers of ethylene glycol units (1–5) for photothermal imaging (Fig. 21). The mitochondria-targeted fluorescent BODIPYs **171–175** form nanoparticles *via* self-assembly in aqueous solution. BODIPYs **171–175** exhibit absorption bands at 639 nm, 648 nm, 648 nm, 648 nm and 648 nm, and emission bands at 646 nm, 661 nm, 659 nm, 662 nm and 660 nm, respectively. The respective BODIPY nanoparticles **171–175** possess photothermal conversion efficiency (η) values of 34.1%, 35.2%, 54.5%, 58.3% and 76.7% (Table 2). BODIPY **175** exhibits a high η as well as a high photoinduced cytotoxicity compared with BODIPYs **171–174**. Nanoparticles of BODIPY **175** can effectively accumulate in tumor sites through the EPR mechanism.[165] In 2019, Qian and co-workers reported the donor–acceptor BODIPY **176** as a sensitizer for intracellular-simulated photodynamic therapy (Fig. 22). BODIPY **176** exhibits a donor triphenylamine unit and acceptor BODIPY unit. BODIPY **176** exhibits an absorption band at 502 nm with a molar extinction coefficient (ε) of 6.18×10^4 M^{-1} cm^{-1}. The emission maximum of BODIPY **176** was observed at 625 nm due to the locally excited state and CT excited state of the donor–acceptor BODIPY. The $^1O_2$ yield of BODIPY **176** is 20.12% (Table 2). Cell viability experiments showed that BODIPY **176** at a concentration of 2–12 μM exhibits low cell cytotoxicity. Intracellular photodynamic therapy studies revealed that BODIPY **176** produces singlet oxygen ($^1O_2$) and kills more than 50% of the cancer cells under irradiation with monochromatic light.[166] Aksakal *et al.* reported the organic–metal-based BODIPYs **177** and **178** and investigated the *in vivo* effects of Ru(II), and Ir(III) BODIPY complexes for PDT, respectively[167] (Fig. 22). The BODIPYs **177** and **178** were synthesized using BODIPY, a phenanthroline group and two distyryl units linked to the BODIPY core. BODIPYs **177** and **178** exhibit three absorption bands, at 352 nm, 579 nm and the characteristic band at 629 nm which is assigned to the $S_0 \rightarrow S_1$ transition. An emission band was observed at 642 nm for both **177** and **178**, and the Stokes shifts were found to be 11–12 nm. The *in vivo* studies suggest that BODIPY **177** is a potential candidate for photodynamic therapy applications compared with BODIPY **178**.

The inhibitory concentration (IC_{50}) of BODIPY **177** was less than 5.0 μM, whereas BODIPY **178** required higher dosages. The Ru(II)-based metal complex BODIPY **177** shows a high $^1O_2$ quantum yield, which makes it a valuable photosensitizer for photodynamic therapy applications (Table 2).[167] In 2019, Xie and co-workers reported the amphiphilic photosensitizer BODIPY **179**, which contains the BODIPY unit and a poly(ethylene glycol) unit connected by thioketal linker for the generation of reactive oxygen species (ROS) (Fig. 22). Nanoparticles of BODIPY **179** provide heat and ROS upon irradiation for PDT applications (Table 2). The BODIPY **179** nanoparticles (10 μM) kill cells through only photothermal effects. To study the thermal properties of BODIPY **179**, the temperature rise and fall of the nanoparticles (NPs) was examined. The incorporation of iodine atoms at the 2- and 6-positions of the BODIPY unit increases the efficiency ISC and generates $^1O_2$ under light irradiation.[158] Recently, Qiao *et al.* reported the

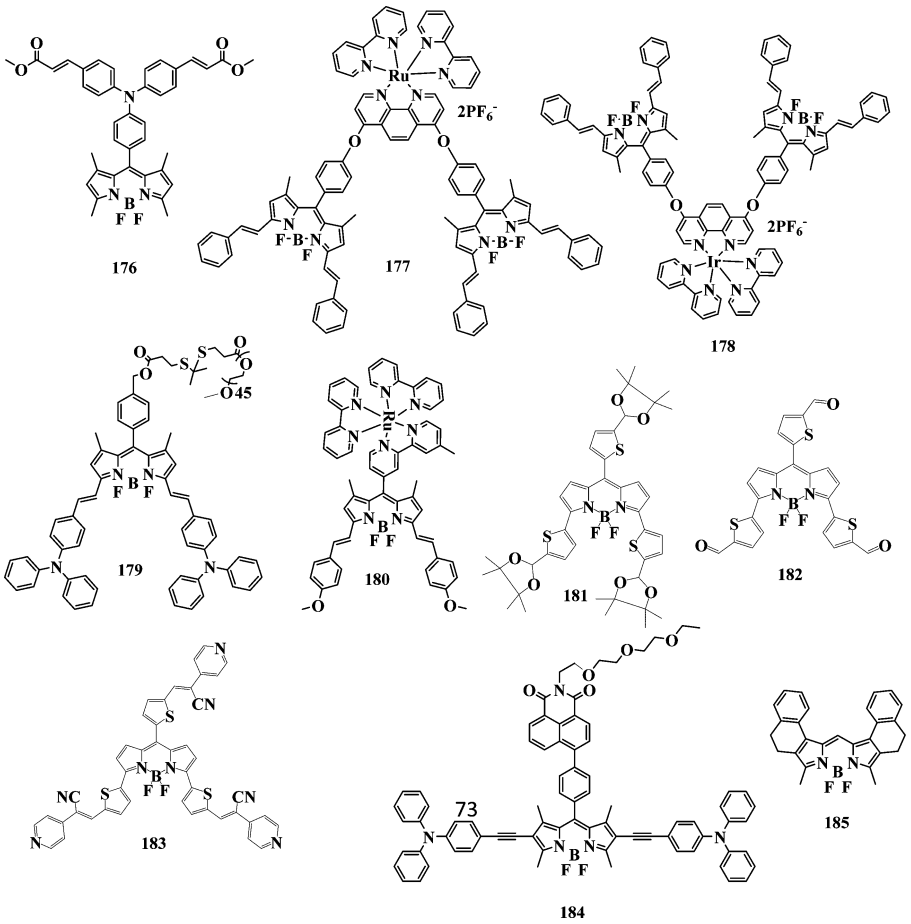

Fig. 22 Molecular structures of BODIPYs **176–185**.

lysosome-targeting, NIR-absorbing Ru(II)-BODIPY **180** for *in vitro* and *in vivo* PDT (Fig. 22). BODIPY **180** was successfully demonstrated for effective PDT against malignant melanoma A375 cells. Photodynamic therapy involves the conversion of oxygen to ROS in the presence of non-toxic photosensitizers (PSs) upon excitation with light, which results in biological responses and causes cell death.

BODIPY **180** shows an absorption band at 652 nm, corresponding to a π–π* transition, with a high molar extinction coefficient (1.2×10^5 M^{-1} cm^{-1}) as well as an emission band at 900 nm, which can be assigned to direct coupling of the ruthenium center with the π-system of distyryl-BODIPY. The $^1O_2$ quantum yield in DMSO was estimated to be 0.77 for BODIPY **180** (Table 2). A375 cells treated with BODIPY **180** showed red fluorescence of the lysosomes, which reveals that the lysosomes were damaged during BODIPY **180**-mediated photodynamic therapy. BODIPY **180** shows striking PDT *in vivo* and is capable of inhibiting tumor growth, indicating that it is a potential candidate for PDT applications.[168] In 2020, Tsumura *et al.* reported a series of BODIPYs **181–183** (Fig. 22) which exhibit an absorption band at 643 nm, 660 nm and 730 nm, and an emission band at 665 nm, 688 nm and 750 nm, respectively, in DCM solvent. Incorporation of the thiophene unit increases the conjugation length, leading to a bathochromic shift in the absorption and emission spectra. The fluorescence quantum yield values of BODIPYs **181–183** are summarized in Table 2.[169] In 2021, Yang *et al.* reported the donor–acceptor–donor (D–A–D)-based BODIPY **184**, which contains BODIPY, 1,8-naphthalimide and triphenylamine units (Fig. 22). The acceptor 1,8-naphthalimide unit was incorporated to enhance the ICT towards the NIR region. The nanoparticles (NPs) of BODIPY **184** exhibit a strong emission at 724 nm and simultaneously generate ROS and heat under single laser irradiation (λ = 635 nm). The NPs of BODIPY **184** are mainly located in the lysosomes of cancer cells. The BODIPY **184** NPs generate ROS and exhibit low toxicity (Table 2). Thus, BODIPY **184** exhibits high stability in aqueous solution and is demonstrated to be a promising nanoagent for cancer treatment.[170] In 2021, Dong *et al.* reported BODIPY **185**, which exhibits an effective $^1O_2$ generation ability under a hypoxic atmosphere (Fig. 22). The twisted molecular structure of BODIPY **185** exhibits high light toxicity (IC_{50} = 1.0 μM) and is a potential photosensitizer for PDT agents. BODIPY **185** exhibits an absorption band at 564 nm ($\varepsilon = 1.2 \times 10^5$ M^{-1} cm^{-1}), which belongs to the $S_0 \rightarrow S_1$ transition, and an absorption band at 350–500 nm, which is attributed to the $S_0 \rightarrow S_2$ and $S_0 \rightarrow S_3$ transitions; in addition, BODIPY **185** exhibits an emission band at 570 nm in the UV-visible spectrum. BODIPY **185** and

2,7-dichlorodihydrofluorescein diacetate (DCF-DA) units are responsible for ROS generation upon light irradiation. Cell death was observed through intracellular ROS generation.[171]

The development of NIR-absorbing BODIPYs has attracted much research attention due to the biological applications of BODIPY derivatives in fluorescence imaging, photodynamic therapy and many more. In PDT applications, the photosensitizer must be light-activated in order to produce reactive oxygen species (ROS). Singlet oxygen ($^1O_2$) is mainly responsible for the cell death induced by PDT.[172] Therefore, the development of most photosensitizers has been focused on enhancing the generation of singlet oxygen ($^1O_2$) species. Several modifications of the BODIPY core have been carried out in order to develop efficient NIR-absorbing BODIPYs for PDT applications, which include the addition of heavy elements, the attachment of electron-withdrawing or electron-donating groups, the design of orthogonal dimers, and the introduction of transition-metal complexes. BODIPYs are valuable photosensitizers because of their remarkable photophysical properties, which include a high intersystem crossing efficiency and singlet oxygen quantum yield, excellent photostability, and low tissue toxicity.[173] Significant research efforts have been devoted to the development of NIR-absorbing BODIPYs for enhancing their performance in PDT, and are as follows:

1. Modification of the core structure of BODIPY or conjugation with metal complexes improves their photophysical properties, which enhances the performance of the photosensitizer in photodynamic therapy (PDT).

2. A popular approach for obtaining NIR-absorbing BODIPYs for photodynamic therapy (PDT) is styryl substitution using the Knoevenagel condensation reaction.

3. To develop NIR-absorbing BODIPYs for PDT applications, the incorporation of electron donor and electron acceptor moieties in D–π–A fashion has been used as a strategy.

4. The attachment of nanocarriers in BODIPYs improves their water solubility and actively delivers the photosensitizer to tumor cells, which enhances the performance of the photosensitizer in PDT applications.

3. Conclusions and prospective futures

The design and synthesis of BODIPY-based D–A materials has been explored extensively because of their tunable electronic and photonic properties, which may be modified by incorporating appropriate donor/acceptor or π-linker groups at the α-, β-pyrrolic or *meso* positions of BODIPY. BODIPY dyes with different substituents, including bromo, iodo, chloro, formyl, vinyl, and amino groups, at the α-, β-pyrrolic or *meso* positions are important building blocks for the development of BODIPY-based π-conjugated donor–acceptor materials. The BODIPY unit exhibits a strong electronic absorption band (covering the visible to the NIR region), high molar extinction coefficients, excellent fluorescence quantum yields, high electron affinities, as well as high photochemical and thermal stabilities. These properties make them suitable candidate for various applications, such as in DSSCs, nonlinear optics (NLOs), hole transporting materials (HTMs), bulk heterojunction solar cells, fluorescent probes, chemosensors, perovskite solar cells (PSCs), photodynamic therapy (PDT) and bioimaging. The HOMO–LUMO gap of BODIPY derivatives can be changed by incorporating various donor and acceptor units at α-, β-pyrrolic and *meso* positions of BODIPY. BODIPY derivatives have been investigated for DSSCs and PDT due to their excellent photostability, high quantum yield and intense light absorption in the UV-vis-NIR region. This review discusses the design, synthesis, functionalization, photophysical and redox properties of BODIPY derivatives and their application in DSSCs and photodynamic therapy (PDT).

Boron dipyrromethane (BODIPY)-based π-conjugated donor–acceptor chromophores have been designed as sensitizers for DSSCs applications. In the BODIPY-based donor–acceptor system, an appropriate electron donor/acceptor group with suitable linkers is a key factor for achieving high power conversion efficiency (η) values. In 2005, Hattori *et al.* reported the BODIPY-based sensitizer 8-(2,4,5-trimethoxyphenyl)-4,4-difluoro-1,3,5,7-tetramethyl-4-bora-3*a*,-4*a*-diaza-*s*-indacene for DSSC applications.[174] The primary benefits of DSSCs over silicon-based solar cells include cheaper production costs, less weight, and flexible processibility. Recent studies have focused on the development of donor–acceptor BODIPYs to enhance the light-harvesting ability. The thermal and photochemical stability, especially the long-term stability and high-power conversion efficiency, of most donor–acceptor-based sensitizers still needs to be researched. BODIPY derivatives can exhibit certain problems in DSSCs, which are as follows:

1. The BODIPY dye exhibits a low power conversion efficiency (0.16%) due to its narrow absorption in the visible region. Without structural modifications, the use of a BODIPY dye results in a poor power conversion efficiency in DSSCs.

2. Insufficient driving force for electron injection. The LUMO energy levels of BODIPY dyes are generally higher than the conduction band (CB) of TiO_2, which may allow effective charge separation at the dye–TiO_2 interface.

3. The significant aggregation of BODIPY dyes on TiO_2 films is a problem that inhibits the photovoltaic performance.[175–177]

Structural modification of the BODIPY dye affects its chemical, physical properties, and photovoltaic performance. The design of D–π–A-type BODIPYs shows good photovoltaic performance. BODIPY units as π-bridges are employed in the development of D–π–A sensitizers, and offer efficient electron communication between the dye and the TiO_2 electrode. To further enhance the photovoltaic performance of D–π–A BODIPYs for DSSCs, more efforts should be devoted to enhancing the light-harvesting ability and electron-injection efficiency.[177] The following points are listed to improve and develop efficient sensitizers for DSSC applications:

1. BODIPY derivatives with red/near-IR absorption should be used as π-bridges in the molecular design of dye sensitizers.

2. Electron-rich chromophores that absorb in the visible region are selected as donors to cover the broad absorption for BODIPY.

3. Conjugation-extended units are used to alter the frontier molecular orbitals of dye sensitizers in order to match the CB of semiconductors and the redox potentials of electrolytes.

4. An appropriate structural arrangement, such as D–π–A–π–A structures, will be more advantageous for electron injection.

5. Aggregation of the sensitizer on the TiO_2 surface must be inhibited to prevent intermolecular energy transfer, which lowers the power conversion efficiency.

6. To enable efficient electron injection and device stability, the sensitizers should have at least one anchoring group (*e.g.*, –COOH, –CNCOOH), which can strongly attach to the TiO_2 surface atoms.

The aim of this review is to provide a general overview of various the BODIPY derivatives used in DSSCs (from 2018 until now) and discuss the major parameters that influence the photovoltaic performance of DSSCs.

Photodynamic therapy (PDT), which uses light and photosensitizing substances, is regarded as an effective therapeutic approach to cancer treatment. BODIPY dyes are excellent photosensitizers because of their excellent photophysical features, which includes high intersystem crossing efficiencies, singlet oxygen ($^1O_2$) quantum yields, good photostability, and low tissue toxicity. BODIPY dyes, which exhibit absorption and emission in the NIR region, are used as potential photosensitizers for PDT without any side effects on healthy cells. By contrast, the structure of BODIPY possesses a few limitations, such as high hydrophobicity, which limits the route of administration. The low stability and low fluorescence of BODIPY produces a low $^1O_2$ generation. It is possible to overcome these limitations by modifying the structure of BODIPY. Such modifications lead to enhanced singlet–triplet intersystem crossing, which generates high $^1O_2$ species and near-infrared-activated BODIPY derivatives for deep tissue penetration.[173] Modified BODIPYs and NIR-absorbing/emitting dyes have attracted a lot of interest, particularly in the fluorescence imaging of targeted organelles and photodynamic therapy. NIR-absorbing dyes exhibit absorption bands in range of 700–900 nm, which is useful for the biological imaging of cells and photodynamic therapy. Herein, we summarized a few significant approaches to synthesize NIR-absorbing BODIPYs for PDT, which are as follows:

1. The incorporation of aryl substituents *via* nucleophilic substitution reactions at the 1-, 3-, 5-, and 7-positions of the BODIPY core enhances redshift.

2. C–C coupling reactions, such as the Suzuki, Stille, Heck and Sonogashira reactions, can be used to synthesize visible- and NIR-absorbing BODIPYs.

3. The oxidative ring fusion of an aromatic system is an effective method that may be utilized in the development of NIR-absorbing BODIPY dyes.

4. The incorporation of electron-donor and electron-acceptor moieties in a D–π–A fashion is appropriate strategy to enhance the bathochromic shift.

5. The incorporation of an N atom at the *meso*-position of BODIPY is a strategy for developing NIR-absorbing BODIPYs.

Photosensitizers (PSs) in photodynamic therapy can transmit light energy to tumor oxygen, generating hazardous reactive oxygen species (ROS), which are employed in the clinical treatment of cancer. This review provides an overview of the design, synthesis and application of BODIPYs in PDT. BODIPY chromophores remain unexplored in different fields, such as organic field-effect transistors, photodynamic therapy, bioimaging, sensors, perovskite solar cells, and many more. The main objectives of this review are to support and encourage researchers to explore the design and synthesis of BODIPY-based D–A chromophores for optoelectronic and bio-applications.

Conflicts of interest

There are no conflicts to declare.

Acknowledgements

I. Y. thanks the Council of Scientific and Industrial Research (CSIR) (File No. 09/1022(0042)/2017-EMR-I), New Delhi for the fellowship. R. M. thanks the Science and Engineering Research Board (SERB) (Project No. CRG/2022/000023) and STR/2022/000001, New Delhi.

References

1 S. Bijesh and R. Misra, *Asian J. Org. Chem.*, 2018, **7**, 1882–1892.
2 S. Garg and N. Goel, *J. Phys. Chem. C*, 2022, **126**, 9313–9323.
3 K. Geramita, Y. Tao, R. A. Segalman and T. D. Tilley, *J. Org. Chem.*, 2010, **75**, 1871–1887.
4 S. Guo, W. Liu, Y. Wu, J. Sun, J. Li, H. Jiang, M. Zhang, S. Wang, Z. Liu, L. Wang, H. Wang, H. Fu and J. Yao, *J. Phys. Chem. Lett.*, 2022, **13**, 7547–7552.
5 T. Ishi-i, K. Ikeda, M. Ogawa and Y. Kusakaki, *RSC Adv.*, 2015, **5**, 89171–89187.
6 K. Kowalski, L. Szczupak, J. Skiba, O. S. Abdel-Rahman, R. F. Winter, R. Czerwieniec and B. Therrien, *Organometallics*, 2014, **33**, 4697–4705.
7 G. Li, Y. Chen, Y. Qiao, Y. Lu and G. Zhou, *J. Org. Chem.*, 2018, **83**, 5577–5587.
8 D. Cappello, F. L. Buguis and J. B. Gilroy, *ACS Omega*, 2022, **7**, 32727–32739.
9 Y. Patil, T. Jadhav, B. Dhokale and R. Misra, *Eur. J. Org. Chem.*, 2016, 733–738.
10 I. S. Yadav, A. Z. Alsaleh, B. Martin, R. Misra and F. D'Souza, *J. Phys. Chem. C*, 2022, **126**, 13300–13310.
11 Y. Rout and R. Misra, *New J. Chem.*, 2021, **45**, 9838–9845.
12 M. Poddar, G. Sivakumar and R. Misra, *J. Mater. Chem. C*, 2019, **7**, 14798–14815.
13 M. Poddar and R. Misra, *Chem. – Asian J.*, 2017, **12**, 2908–2915.
14 B. Dhokale, T. Jadhav, S. M. Mobin and R. Misra, *RSC Adv.*, 2015, **5**, 57692–57699.
15 Y. Rout, P. Gautam and R. Misra, *J. Org. Chem.*, 2017, **82**, 6840–6845.
16 D. Zhang and M. Heeney, *Asian J. Org. Chem.*, 2020, **9**, 1251.

17 P. Gautam, R. Misra and G. D. Sharma, *Phys. Chem. Chem. Phys.*, 2016, **18**, 7235–7241.
18 V. Piradi, Y. Gao, F. Yan, M. Imran, J. Zhao, X. Zhu and S. K. So, *ACS Appl. Energy Mater.*, 2022, **5**, 7287–7296.
19 Y. Patil, R. Misra, A. Sharma and G. D. Sharma, *Phys. Chem. Chem. Phys.*, 2016, **18**, 16950–16957.
20 R. Maragani, R. Sharma and R. Misra, *ChemistrySelect*, 2017, **2**, 10033–10037.
21 Y. Rout, Y. Jang, H. B. Gobeze, R. Misra and F. D'Souza, *J. Phys. Chem. C*, 2019, **123**, 23382–23389.
22 S. Li, M. He, X. Jin, W. Geng, C. Li, X. Li, Z. Zhang, J. Qian and J. Hua, *Chem. Mater.*, 2022, **34**, 5999–6008.
23 Y. Zhao, Z. Zhang, Z. Lu, H. Wang and Y. Tang, *ACS Appl. Mater. Interfaces*, 2019, **11**, 38467–38474.
24 K. Tram, H. Yan, H. A. Jenkins, S. Vassiliev and D. Bruce, *Dyes Pigm.*, 2009, **82**, 392–395.
25 J. Shinde, M. B. Thomas, M. Poddar, R. Misra and F. D'Souza, *J. Phys. Chem. C*, 2021, **125**, 23911–23921.
26 R. Maragani, M. B. Thomas, R. Misra and F. D'Souza, *J. Phys. Chem. A*, 2018, **122**, 4829–4837.
27 V. Lakshmi, M. R. Rao and M. Ravikanth, *Org. Biomol. Chem.*, 2015, **13**, 2501–2517.
28 N. Boens, V. Leen and W. Dehaen, *Chem. Soc. Rev.*, 2012, **41**, 1130–1172.
29 E. Fron, E. Coutiño-Gonzalez, L. Pandey, M. Sliwa, M. V. der Auweraer, F. C. D. Schryver, J. Thomas, Z. Dong, V. Leen, M. Smet, W. Dehaen and T. Vosch, *New J. Chem.*, 2009, **33**, 1490–1496.
30 J. Miao, Y. Wang, J. Liu and L. Wang, *Chem. Soc. Rev.*, 2022, **51**, 153–187.
31 A. Treibs and F.-H. Kreuzer, *Justus Liebigs Ann. Chem.*, 1968, **718**, 208–223.
32 B. Carlotti, M. Poddar, F. Elisei, A. Spalletti and R. Misra, *J. Phys. Chem. C*, 2019, **123**, 24362–24374.
33 R. Misra, B. Dhokale, T. Jadhav and S. M. Mobin, *Organometallics*, 2014, **33**, 1867–1877.
34 B. Shen and Y. Qian, *J. Mater. Chem. B*, 2016, **4**, 7549–7559.
35 Z. Zhou and T. Maki, *J. Org. Chem.*, 2021, **86**, 17560–17566.
36 B. Dhokale, T. Jadhav, S. M. Mobin and R. Misra, *Chem. Commun.*, 2014, **50**, 9119–9121.
37 N. O. Didukh, V. P. Yakubovskyi, Y. V. Zatsikha, G. T. Rohde, V. N. Nemykin and Y. P. Kovtun, *J. Org. Chem.*, 2019, **84**, 2133–2147.
38 A. B. Nepomnyashchii, M. Bröring, J. Ahrens and A. J. Bard, *J. Am. Chem. Soc.*, 2011, **133**, 8633–8645.
39 C. O. Obondi, G. N. Lim, P. A. Karr, V. N. Nesterov and F. D'Souza, *Phys. Chem. Chem. Phys.*, 2016, **18**, 18187–18200.
40 S. G. Awuah and Y. You, *RSC Adv.*, 2012, **2**, 11169–11183.
41 Y. Qin, X. Liu, P.-P. Jia, L. Xu and H.-B. Yang, *Chem. Soc. Rev.*, 2020, **49**, 5678–5703.
42 B. T. Aksoy, B. Dedeoglu, Y. Zorlu, M. M. Ayhan and B. Çoş ut, *CrystEngComm*, 2022, **24**, 5630–5641.
43 P. Li, F. Wu, Y. Fang, H. Dahiya, M. L. Keshtov, H. Xu, A. Agrawal and G. D. Sharma, *ACS Appl. Energy Mater.*, 2022, **5**, 2279–2289.
44 S. Gangada, R. A. Ramnagar, A. A. Sangolkar, R. Pawar, J. B. Nanubolu, P. Roy, L. Giribabu and R. Chitta, *J. Phys. Chem. A*, 2020, **124**, 9738–9750.
45 R. Misra, B. Dhokale, T. Jadhav and S. M. Mobin, *Dalton Trans.*, 2014, **43**, 4854–4861.
46 B. Umasekhar, E. Ganapathi, T. Chatterjee and M. Ravikanth, *Dalton Trans.*, 2015, **44**, 16516–16527.
47 Y. Chen, J. Zhao, H. Guo and L. Xie, *J. Org. Chem.*, 2012, **77**, 2192–2206.
48 M. R. Rao, K. V. P. Kumar and M. Ravikanth, *J. Organomet. Chem.*, 2010, **695**, 863–869.
49 P. Gautam, B. Dhokale, S. M. Mobin and R. Misra, *RSC Adv.*, 2012, **2**, 12105–12107.
50 D. Collado, J. Casado, S. R. González, J. T. L. Navarrete, R. Suau, E. Perez-Inestrosa, T. M. Pappenfus and M. M. M. Raposo, *Chem. – Eur. J.*, 2011, **17**, 498–507.
51 M. E. El-Khouly, S. Fukuzumi and F. D'Souza, *Chem. Phys. Chem.*, 2014, **15**, 30–47.
52 B. Dhokale, T. Jadhav, S. M. Mobin and R. Misra, *J. Org. Chem.*, 2015, **80**, 8018–8025.
53 T. Mikulchyk, S. Karuthedath, C. S. P. D. Castro, A. A. Buglak, A. Sheehan, A. Wieder, F. Laquai, I. Naydenova and M. A. Filatov, *J. Mater. Chem. C*, 2022, **10**, 11588–11597.
54 E. Bassan, A. Gualandi, P. G. Cozzi and P. Ceroni, *Chem. Sci.*, 2021, **12**, 6607–6628.
55 J. M. Merkes, T. Ostlender, F. Wang, F. Kiessling, H. Sun and S. Banala, *New J. Chem.*, 2021, **45**, 19641–19645.
56 F. An, J. Xin, C. Deng, X. Tan, O. Aras, N. Chen, X. Zhang and R. Ting, *J. Mater. Chem. B*, 2021, **9**, 9308–9315.
57 X. Liu, W. Chi, Q. Qiao, S. V. Kokate, E. P. Cabrera, Z. Xu, X. Liu and Y.-T. Chang, *ACS Sens.*, 2020, **5**, 731–739.
58 L. Sansalone, S. Tang, J. Garcia-Amorós, Y. Zhang, S. Nonell, J. D. Baker, B. Captain and F. M. Raymo, *ACS Sens.*, 2018, **3**, 1347–1353.
59 C.-C. Chi, Y.-J. Huang and C.-T. Chen, *J. Chin. Chem. Soc.*, 2012, **59**, 305–316.
60 I. Bulut, Q. Huaulmé, A. Mirloup, P. Chávez, S. Fall, A. Hébraud, S. Méry, B. Heinrich, T. Heiser, P. Lévêque and N. Leclerc, *ChemSusChem*, 2017, **10**, 1878–1882.
61 J. Zhao, K. Xu, W. Yang, Z. Wang and F. Zhong, *Chem. Soc. Rev.*, 2015, **44**, 8904–8939.
62 B. Li, T. Xu, X. Wang, S. Zhao, B. Wang, L. Jiang, X. Song and M. Lan, *J. Innovative Opt. Health Sci.*, 2022, **15**, 2240006.
63 I. Esnal, A. Urías-Benavides, C. F. A. Gómez-Durán, C. A. Osorio-Martínez, I. García-Moreno, A. Costela, J. Bañuelos, N. Epelde, I. López Arbeloa, R. Hu, B. Zhong Tang and E. Peña-Cabrera, *Chem. – Asian J.*, 2013, **8**, 2691–2700.
64 J. H. Boyer, A. M. Haag, G. Sathyamoorthi, M.-L. Soong, K. Thangaraj and T. G. Pavlopoulos, *Heteroat. Chem.*, 1993, **4**, 39–49.
65 M. Zhang, E. Hao, Y. Xu, S. Zhang, H. Zhu, Q. Wang, C. Yu and L. Jiao, *RSC Adv.*, 2012, **2**, 11215–11218.
66 L. Jiao, C. Yu, J. Wang, E. A. Briggs, N. A. Besley, D. Robinson, M. J. Ruedas-Rama, A. Orte, L. Crovetto,

E. M. Talavera, J. M. Alvarez-Pez, M. V. der Auweraer and N. Boens, *RSC Adv.*, 2015, **5**, 89375–89388.
67 S. Kolemen, Y. Cakmak, Z. Kostereli and E. U. Akkaya, *Org. Lett.*, 2014, **16**, 660–663.
68 D. Kim, K. Yamamoto and K. H. Ahn, *Tetrahedron*, 2012, **68**, 5279–5282.
69 W. Chi, Q. Qiao, R. Lee, W. Liu, Y. S. Teo, D. Gu, M. J. Lang, Y.-T. Chang, Z. Xu and X. Liu, *Angew. Chem., Int. Ed.*, 2019, **58**, 7073–7077.
70 N. Boens, B. Verbelen, M. J. Ortiz, L. Jiao and W. Dehaen, *Coord. Chem. Rev.*, 2019, **399**, 213024.
71 N. Boens, V. Leen, W. Dehaen, L. Wang, K. Robeyns, W. Qin, X. Tang, D. Beljonne, C. Tonnelé, J. M. Paredes, M. J. Ruedas-Rama, A. Orte, L. Crovetto, E. M. Talavera and J. M. Alvarez-Pez, *J. Phys. Chem. A*, 2012, **116**, 9621–9631.
72 N. Boens, B. Verbelen and W. Dehaen, *Eur. J. Org. Chem.*, 2015, 6577–6595.
73 S. Zhu, J. Bi, G. Vegesna, J. Zhang, F.-T. Luo, L. Valenzano and H. Liu, *RSC Adv.*, 2013, **3**, 4793–4800.
74 J.-M. Ji, H. Zhou and H. K. Kim, *J. Mater. Chem. A*, 2018, **6**, 14518–14545.
75 S. Hattori, K. Ohkubo, H. Urano, T. Nagano, Y. Wada, N. V. Tkachenko, H. Lemmetyinen and S. Fukuzumi, *J. Phys. Chem. B*, 2005, **109**, 15368–15375.
76 T. Rohand, M. Baruah, W. Qin, N. Boens and W. Dehaen, *Chem. Commun.*, 2006, 266–268.
77 N. Boens, B. Verbelen, M. J. Ortiz, L. Jiao and W. Dehaen, *Coord. Chem. Rev.*, 2019, **399**, 213024.
78 G. Meng, S. Velayudham, A. Smith, R. Luck and H. Liu, *Macromolecules*, 2009, **42**, 1995–2001.
79 H. Lu, Q. Wang, L. Gai, Z. Li, Y. Deng, X. Xiao, G. Lai and Z. Shen, *Chem. – Eur. J.*, 2012, **18**, 7852–7861.
80 V. Leen, P. Yuan, L. Wang, N. Boens and W. Dehaen, *Org. Lett.*, 2012, **14**, 6150–6153.
81 Y. Zhang, X. Shao, Y. Wang, F. Pan, R. Kang, F. Peng, Z. Huang, W. Zhang and W. Zhao, *Chem. Commun.*, 2015, **51**, 4245–4248.
82 S. Madhu, M. R. Rao, M. S. Shaikh and M. Ravikanth, *Inorg. Chem.*, 2011, **50**, 4392–4400.
83 S. Madhu, S. Kumar, T. Chatterjee and M. Ravikanth, *New J. Chem.*, 2014, **38**, 5551–5558.
84 X. Zhang, Y. Zhang, L. Chen and Y. Xiao, *RSC Adv.*, 2015, **5**, 32283–32289.
85 C. O. Obondi, G. N. Lim, P. A. Karr, V. N. Nesterov and F. D'Souza, *Phys. Chem. Chem. Phys.*, 2016, **18**, 18187–18200.
86 J. Shinde, M. B. Thomas, M. Poddar, R. Misra and F. D'Souza, *J. Phys. Chem. C*, 2021, **125**, 23911–23921.
87 M. R. Rao, K. V. P. Kumar and M. Ravikanth, *J. Organomet. Chem.*, 2010, **695**, 863–869.
88 V. Lakshmi and M. Ravikanth, *Dyes Pigm.*, 2013, **96**, 665–671.
89 S. Wanwong, P. Khomein and S. Thayumanavan, *Chem. Cent. J.*, 2018, **12**, 60.
90 S. Kim, Y. Zhou, N. Tohnai, H. Nakatsuji, M. Matsusaki, M. Fujitsuka, M. Miyata and T. Majima, *Chem. – Eur. J.*, 2018, **24**, 636–645.
91 A. Mirloup, N. Leclerc, S. Rihn, T. Bura, R. Bechara, A. Hébraud, P. Lévêque, T. Heiser and R. Ziessel, *New J. Chem.*, 2014, **38**, 3644–3653.
92 J. Liao, H. Zhao, Y. Xu, Z. Cai, Z. Peng, W. Zhang, W. Zhou, B. Li, Q. Zong and X. Yang, *Dyes Pigm.*, 2016, **128**, 131–140.
93 Q. Huaulmé, S. Fall, P. Lévêque, G. Ulrich and N. Leclerc, *Chem. – Eur. J.*, 2019, **25**, 6613–6620.
94 F. J. Frank, P. G. Waddell, M. J. Hall and J. G. Knight, *Org. Lett.*, 2021, **23**, 8595–8599.
95 Z. Feng, L. Jiao, Y. Feng, C. Yu, N. Chen, Y. Wei, X. Mu and E. Hao, *J. Org. Chem.*, 2016, **81**, 6281–6291.
96 H. Zhang, X. Chen, J. Lan, Y. Liu, F. Zhou, D. Wu and J. You, *Chem. Commun.*, 2018, **54**, 3219–3222.
97 S. Goeb and R. Ziessel, *Org. Lett.*, 2007, **9**, 737–740.
98 L. Bonardi, G. Ulrich and R. Ziessel, *Org. Lett.*, 2008, **10**, 2183–2186.
99 T. Rousseau, A. Cravino, E. Ripaud, P. Leriche, S. Rihn, A. D. Nicola, R. Ziessel and J. Roncali, *Chem. Commun.*, 2010, **46**, 5082–5084.
100 S. Rihn, M. Erdem, A. De Nicola, P. Retailleau and R. Ziessel, *Org. Lett.*, 2011, **13**, 1916–1919.
101 T. Freese, L. J. Patalag, J. L. Merz, P. G. Jones and D. B. Werz, *J. Org. Chem.*, 2021, **86**, 3089–3095.
102 L. J. Patalag, P. G. Jones and D. B. Werz, *Angew. Chem., Int. Ed.*, 2016, **55**, 13340–13344.
103 L. J. Patalag, M. Loch, P. G. Jones and D. B. Werz, *J. Org. Chem.*, 2019, **84**, 7804–7814.
104 I.-S. Tamgho, A. Hasheminasab, J. T. Engle, V. N. Nemykin and C. J. Ziegler, *J. Am. Chem. Soc.*, 2014, **136**, 5623–5626.
105 F. Lv, D. Liu, W. Zheng, Y. Zhao and F. Song, *ACS Appl. Nano Mater.*, 2021, **4**, 6012–6019.
106 C. He, H. Zhou, N. Yang, N. Niu, E. Hussain, Y. Li and C. Yu, *New J. Chem.*, 2018, **42**, 2520–2525.
107 X.-D. Jiang, Y. Su, S. Yue, C. Li, H. Yu, H. Zhang, C.-L. Sun and L.-J. Xiao, *RSC Adv.*, 2015, **5**, 16735–16739.
108 R. Hasegawa, S. Iwakiri and Y. Kubo, *New J. Chem.*, 2021, **45**, 6091–6099.
109 J. Wang, Q. Wu, C. Yu, Y. Wei, X. Mu, E. Hao and L. Jiao, *J. Org. Chem.*, 2016, **81**, 11316–11323.
110 Q. Huaulmé, A. Mirloup, P. Retailleau and R. Ziessel, *Org. Lett.*, 2015, **17**, 2246–2249.
111 I.-S. Tamgho, A. Hasheminasab, J. T. Engle, V. N. Nemykin and C. J. Ziegler, *J. Am. Chem. Soc.*, 2014, **136**, 5623–5626.
112 J. S. Dhindsa, F. L. Buguis, M. Anghel and J. B. Gilroy, *J. Org. Chem.*, 2021, **86**, 12064–12074.
113 J. D. B. Koenig, M. E. Farahat, J. S. Dhindsa, J. B. Gilroy and G. C. Welch, *Mater. Chem. Front.*, 2020, **4**, 1643–1647.
114 C. Kumar, A. R. Agrawal, N. G. Ghosh, H. S. Karmakar, S. Das, N. R. Kumar, V. W. Banewar and S. S. Zade, *Dalton Trans.*, 2020, **49**, 13202–13206.
115 S. M. Barbon, J. T. Price, U. Yogarajah and J. B. Gilroy, *RSC Adv.*, 2015, **5**, 56316–56324.
116 S. M. Barbon, J. V. Buddingh, R. R. Maar and J. B. Gilroy, *Inorg. Chem.*, 2017, **56**, 12003–12011.

117 M. Hesari, S. M. Barbon, R. B. Mendes, V. N. Staroverov, Z. Ding and J. B. Gilroy, *J. Phys. Chem. C*, 2018, **122**, 1258–1266.
118 B. O'Regan and M. Grätzel, *Nature*, 1991, **353**, 737–740.
119 M. Mao, X.-L. Zhang, X.-Q. Fang, G.-H. Wu, Y. Ding, X.-L. Liu, S.-Y. Dai and Q.-H. Song, *Org. Electron.*, 2014, **15**, 2079–2090.
120 H. Liu, L. Liu, Y. Fu, E. Liu and B. Xue, *J. Chem. Inf. Model.*, 2019, **59**, 2248–2256.
121 K. Sharma, V. Sharma and S. S. Sharma, *Nanoscale Res. Lett.*, 2018, **13**, 381.
122 A. M. Poe, A. M. D. Pelle, A. V. Subrahmanyam, W. White, G. Wantz and S. Thayumanavan, *Chem. Commun.*, 2014, **50**, 2913–2915.
123 L. Bucher, N. Desbois, P. D. Harvey, C. P. Gros, R. Misra and G. D. Sharma, *ACS Appl. Energy Mater.*, 2018, **1**, 3359–3368.
124 B. Liu, Z. Ma, Y. Xu, Y. Guo, F. Yang, D. Xia, C. Li, Z. Tang and W. Li, *J. Mater. Chem. C*, 2020, **8**, 2232–2237.
125 A. Soultati, A. Verykios, S. Panagiotakis, K.-K. Armadorou, M. I. Haider, A. Kaltzoglou, C. Drivas, A. Fakharuddin, X. Bao, C. Yang, A. R. bin, M. Yusoff, E. K. Evangelou, I. Petsalakis, S. Kennou, P. Falaras, K. Yannakopoulou, G. Pistolis, P. Argitis and M. Vasilopoulou, *ACS Appl. Mater. Interfaces*, 2020, **12**, 21961–21973.
126 S.-C. Yeh, L.-J. Wang, H.-M. Yang, Y.-H. Dai, C.-W. Lin, C.-T. Chen and R.-J. Jeng, *Chem. – Eur. J.*, 2017, **23**, 14747–14759.
127 S. Erten-Ela, Y. Ueno, T. Asaba and Y. Kubo, *New J. Chem.*, 2017, **41**, 10367–10375.
128 Y. Kubota, K. Kimura, J. Jin, K. Manseki, K. Funabiki and M. Matsui, *New J. Chem.*, 2019, **43**, 1156–1165.
129 M. F. Shah, A. Mirloup, T. H. Chowdhury, S. Alexandra, A. S. Hanbazazah, A. Ahmed, J.-J. Lee, N. Leclerc, M. Abdel-Shakour and A. Islam, *Sustainable Energy Fuels*, 2019, **3**, 2983–2989.
130 N. T. Z. Potts, T. Sloboda, M. Wächtler, R. A. Wahyuono, V. D'Annibale, B. Dietzek, U. B. Cappel and E. A. Gibson, *J. Chem. Phys.*, 2020, **153**, 184704.
131 S. Wanwong, W. Sangkhun and J. Wootthikanokkhan, *RSC Adv.*, 2018, **8**, 9202–9210.
132 M. Mao, X.-L. Zhang and G.-H. Wu, *Int. J. Photoenergy*, 2018, **2018**, 1–9.
133 M. F. Shah, A. Mirloup, T. H. Chowdhury, A. Sutter, A. S. Hanbazazah, A. Ahmed, J.-J. Lee, M. Abdel-Shakour, N. Leclerc, R. Kaneko and A. Islam, *Sustainable Energy Fuels*, 2020, **4**, 1908–1914.
134 A. U. Rahman, M. B. Khan, M. Yaseen and G. Rahman, *ACS Omega*, 2021, **6**, 27640–27653.
135 E. A. Yildiz, G. Sevinc, H. G. Yaglioglu and M. Hayvali, *J. Photochem. Photobiol., A*, 2019, **375**, 148–157.
136 E. A. Yildiz, G. Sevinc, H. G. Yaglioglu and M. Hayvali, *Opt. Mater.*, 2019, **91**, 50–57.
137 V. Saravanan, S. Ganesan and P. Rajakumar, *RSC Adv.*, 2020, **10**, 18390–18399.
138 J. Babu, S. Ganesan, M. Karuppusamy and P. Rajakumar, *ChemistrySelect*, 2018, **3**, 9222–9231.
139 P. Chinna Ayya Swamy, G. Sivaraman, R. N. Priyanka, S. O. Raja, K. Ponnuvel, J. Shanmugpriya and A. Gulyani, *Coord. Chem. Rev.*, 2020, **411**, 213233.
140 N. Epelde-Elezcano, E. Palao, H. Manzano, A. Prieto-Castañeda, A. R. Agarrabeitia, A. Tabero, A. Villanueva, S. de la Moya, Í. López-Arbeloa, V. Martínez-Martínez and M. J. Ortiz, *Chem. – Eur. J.*, 2017, **23**, 4837–4848.
141 Y. Cakmak, S. Kolemen, S. Duman, Y. Dede, Y. Dolen, B. Kilic, Z. Kostereli, L. T. Yildirim, A. L. Dogan, D. Guc and E. U. Akkaya, *Angew. Chem., Int. Ed.*, 2011, **50**, 11937–11941.
142 B. Ventura, G. Marconi, M. Bröring, R. Krüger and L. Flamigni, *New J. Chem.*, 2009, **33**, 428–438.
143 B. Gu, W. Wu, G. Xu, G. Feng, F. Yin, P. H. J. Chong, J. Qu, K.-T. Yong and B. Liu, *Adv. Mater.*, 2017, **29**, 1701076.
144 J. Xiao, H. Cong, S. Wang, B. Yu and Y. Shen, *Biomater. Sci.*, 2021, **9**, 2384–2412.
145 G. Ulrich, R. Ziessel and A. Harriman, *Angew. Chem., Int. Ed.*, 2008, **47**, 1184–1201.
146 A. Loudet and K. Burgess, *Chem. Rev.*, 2007, **107**, 4891–4932.
147 P. Chinna Ayya Swamy, G. Sivaraman, R. N. Priyanka, S. O. Raja, K. Ponnuvel, J. Shanmugpriya and A. Gulyani, *Coord. Chem. Rev.*, 2020, **411**, 213233.
148 A. Kamkaew, S. H. Lim, H. B. Lee, L. V. Kiew, L. Y. Chung and K. Burgess, *Chem. Soc. Rev.*, 2012, **42**, 77–88.
149 Y. Liu, C. Xu, L. Teng, H.-W. Liu, T.-B. Ren, S. Xu, X. Lou, H. Guo, L. Yuan and X.-B. Zhang, *Chem. Commun.*, 2020, **56**, 1956–1959.
150 Y. Su, S. Lu, P. Gao, M. Zheng and Z. Xie, *Mater. Chem. Front.*, 2019, **3**, 1747–1753.
151 Z. Chang, J.-H. Ye, F. Qi, H. Fang, F. Lin, S. Wang, C. Mu, W. Zhang and W. He, *New J. Chem.*, 2021, **45**, 6180–6185.
152 X. Guo, R. C. H. Wong, Y. Zhou, D. K. P. Ng and P.-C. Lo, *Chem. Commun.*, 2019, **55**, 13518–13521.
153 J. Zhu, J. Zou, J. Zhang, Y. Sun, X. Dong and Q. Zhang, *J. Mater. Chem. B*, 2019, **7**, 3303–3309.
154 S. Radunz, S. Wedepohl, M. Röhr, M. Calderón, H. R. Tschiche and U. Resch-Genger, *J. Med. Chem.*, 2020, **63**, 1699–1708.
155 E. Jung, I. Shim, J. An, M. S. Ji, P. Jangili, S.-G. Chi and J. S. Kim, *ACS Appl. Bio Mater.*, 2021, **4**, 2120–2127.
156 Q. Liu, J. Tian, Y. Tian, Q. Sun, D. Sun, F. Wang, H. Xu, G. Ying, J. Wang, A. K. Yetisen and N. Jiang, *ACS Nano*, 2021, **15**, 515–525.
157 C. Wang and Y. Qian, *Org. Biomol. Chem.*, 2019, **17**, 8001–8007.
158 C. Li, W. Lin, S. Liu, W. Zhang and Z. Xie, *J. Mater. Chem. B*, 2019, **7**, 4655–4660.
159 B. Hwang, T.-I. Kim, H. Kim, S. Jeon, Y. Choi and Y. Kim, *J. Mater. Chem. B*, 2021, **9**, 824–831.
160 A. Garai, A. Gandhi, V. Ramu, M. K. Raza, P. Kondaiah and A. R. Chakravarty, *ACS Omega*, 2018, **3**, 9333–9338.
161 H. Wang, W. Zhao, X. Liu, S. Wang and Y. Wang, *ACS Appl. Bio Mater.*, 2020, **3**, 593–601.
162 C. Wang and Y. Qian, *Biomater. Sci.*, 2020, **8**, 830–836.

163 G. Turkoglu, G. K. Koygun, M. N. Z. Yurt, N. Demirok and S. Erbas-Cakmak, *Org. Biomol. Chem.*, 2020, **18**, 9433–9437.
164 V. Ramu, P. Kundu, P. Kondaiah and A. R. Chakravarty, *Inorg. Chem.*, 2021, **60**, 6410–6420.
165 J.-L. Wang, L. Zhang, M.-J. Zhao, T. Zhang, Y. Liu and F.-L. Jiang, *ACS Appl. Bio Mater.*, 2021, **4**, 1760–1770.
166 L. Wang, J. Bai and Y. Qian, *New J. Chem.*, 2019, **43**, 16829–16834.
167 N. E. Aksakal, E. T. Eçik, H. H. Kazan, G. Y. Çiftçi and F. Yuksel, *Photochem. Photobiol. Sci.*, 2019, **18**, 2012–2022.
168 L. Qiao, J. Liu, Y. Han, F. Wei, X. Liao, C. Zhang, L. Xie, L. Ji and H. Chao, *Chem. Commun.*, 2021, **57**, 1790–1793.
169 S. Tsumura, K. Ohira, K. Hashimoto, K. Imato and Y. Ooyama, *Mater. Chem. Front.*, 2020, **4**, 2762–2771.
170 M. Yang, J. Deng, H. Su, S. Gu, J. Zhang, A. Zhong and F. Wu, *Mater. Chem. Front.*, 2021, **5**, 406–417.
171 Y. Dong, P. Kumar, P. Maity, I. Kurganskii, S. Li, A. Elmali, J. Zhao, D. Escudero, H. Wu, A. Karatay, O. F. Mohammed and M. Fedin, *Phys. Chem. Chem. Phys.*, 2021, **23**, 8641–8652.
172 S. G. Awuah and Y. You, *RSC Adv.*, 2012, **2**, 11169–11183.
173 C. S. Kue, S. Y. Ng, S. H. Voon, A. Kamkaew, L. Y. Chung, L. V. Kiew and H. B. Lee, *Photochem. Photobiol. Sci.*, 2018, **17**, 1691–1708.
174 S. Hattori, K. Ohkubo, Y. Urano, H. Sunahara, T. Nagano, Y. Wada, N. V. Tkachenko, H. Lemmetyinen and S. Fukuzumi, *J. Phys. Chem. B*, 2005, **109**, 15368–15375.
175 H. Klfout, A. Stewart, M. Elkhalifa and H. He, *ACS Appl. Mater. Interfaces*, 2017, **9**, 39873–39889.
176 C. Qin, A. Mirloup, N. Leclerc, A. Islam, A. El-Shafei, L. Han and R. Ziessel, *Adv. Energy Mater.*, 2014, **4**, 1400085.
177 M. Mao and Q.-H. Song, *Chem. Rec.*, 2016, **16**, 719–733.